Studies on electrical spin injection and spin transport in organic materials

TAKESHI KAMIYA

MARCH 2017

Studies on electrical spin injection and spin transport in organic materials

A dissertation submitted to
THE GRADUATE SCHOOL OF ENGINEERING SCIENCE
OSAKA UNIVERSITY
in partial fulfillment of the requirements for the degree of
DOCTOR OF PHILOSOPHY IN ENGINEERING

BY

TAKESHI KAMIYA

MARCH 2017

Abstract

There have been growing interests in the electrical spin injection and spin transport in organic materials (OMs) since low spin-orbit interaction of OMs leads long spin relaxation times. However, spin transport properties of OMs have been still unclear since previous studies are based on layered device structures where spin polarized current includes spurious effects such as interface magnetoresistance (MR). For better understanding of spin transport, it is mandatory to separate the spin current from the charge current in OMs by the used of nonlocal spin valves. Similarly, interface MR should be investigated independently against spin transport properties in OMs.

In this thesis, nonlocal spin valves based on an organic multilayered zero-gap conductor α-(BEDT-TTF)$_2$I$_3$ were prepared, in which the spin current was well separated form the charge current. The nonlocal MR observed in this study showed intrinsic spin transport properties of α-(BEDT-TTF)$_2$I$_3$, and the spin diffusion length and the spin relaxation time at 2.5 K were evaluated to be 1.1 μm and 3 ns, respectively. Experimental results suggest that multilayered structure of α-(BEDT-TTF)$_2$I$_3$ suppress the spin scattering from the surface and the substrate, resulting in the long spin relaxation time. These findings provide guiding principles for materials design in organic spintronics.

Next, this thesis discusses tunneling anisotropic magnetoresistance (TAMR) at the interface between the OMs and the ferromagnetic (FM) electrode by using the devices consisting of FM/OMs/Cu layers. Experimental results showed that the magnetic field dependence of the TAMR was changed strongly by choosing the substrate on which the FM electrode were grown. This result implies that active control of the interface magnetic anisotropy between the OMs and the FM electrodes can increase the interface MR, which promotes the development of functional organic spin valves.

Table of contents

Chapter 1

Introduction

This chapter will present a brief history and current stage of the research field of spintronics.

1.1 Spintronics

In their textbook "Introduction to Spintronics" 2008,[1] Bandyopadhyay and Cahay explain spintronics as follows: it deals primarily with the science and technology of using the spin degree of freedom of a charge carrier to store, encode, access, process and/or transmit information in some way. In other words, spintronics is a technological field of science that attempts to develop high density, high speed, energy saving devices by manipulating the charge and spin degrees of freedom of electrons simultaneously. Spintronics is applied to optical,[2, 3] thermal,[4, 5] and dynamical methods[6, 7] as well as electrical methods[8, 9] to control the spin degrees of freedom of electrons.

The first discovery of the spintronic phenomenon was the anisotropic magnetoresistance (AMR) in 1856,[10] which is the change in the resistance of ferromagnetic metals depending on the magnetization direction with respect to the direction of the electrical current. There has been an even greater interest in the study of spintronics following the discovery of giant magnetoresistance (GMR) in 1988 by Fert et al.[8] and by Grünberg et al.[9] GMR is derived from the "spin valve" concept[1] that is used to investigate the properties associated with spin injection and spin transport in nonmagnetic materials. Note that the spin valve is an important device from the perspective of fundamental spin physics and device applications. It enables ways to

electrically manipulate charge and spin degrees of freedom of electrons in spin polarized current injected from the ferromagnetic metal (FM) electrode. One of the most fundamental technological applications in spintronics has been the fabrication of devices based on the GMR effect that are used in the development of magnetic storage media, such as read-head sensors for computer hard disks. The discovery of GMR has been recognized as an important advance in basic science, receiving the Nobel Prize in Physics (2007). A description of the primary concepts of the spin valve will follow in the next section.

Currently, the research field of spintronics expanded and novel achievements have been made, such as the demonstration of the spin-Seebeck effect,[4, 5] spin-charge current convertors,[6, 7] spin torque diodes,[11] spin field effect transistors[12] Other practical applications with the spin valve are magnetic random access memory (MRAM) and the spin transfer torque random access memory (STT-MRAM), which are expected to be universally used in future storage devices combining low-cost, high-speed, non-volatility, with better durability.

1.2 Spin valve

1.2.1 A simple two resistor model

The spin valve device (SV) is widely used for measurement of the spin injection and the spin transport properties in nonmagnetic metals, semiconductors and even in organic materials (OMs).[13] SVs basically consist of thin nonmagnetic materials (spacers) sandwiched between two FM electrodes, as shown in Figs. 1.1(a) and 1.1(b) (the magnetization direction of FMs is indicated by red/blue arrows). According to a two-current model described by Mott,[14] the total current $\boldsymbol{J}$ in ferromagnetic materials can be

divided into majority and minority spin current since no mixing occurs between them in the absence of spin flip scattering. It is given by

$$\boldsymbol{J} = \boldsymbol{J}_1 + \boldsymbol{J}_2,$$

where $\boldsymbol{J}_1$ and $\boldsymbol{J}_2$ represent the current of minority spin and majority spin, respectively. An electron having spin parallel (or antiparallel) to the magnetization of ferromagnetic materials is a majority (or minority) spin. Because band structures for each spin direction in FMs are different, electrons for a fixed energy in FMs have different momentum depending on their own spin directions. The resistance of majority spin current is different from that of minority spin current. Thus, one can estimate the resistance of the spin valve device using the resistor network model depicted in Figs. 1.1(c) and 1.1(d). The total resistance of the spin valve is the parallel combination of the resistances written as follows

$$R_P = \frac{(2R_\uparrow)(2R_\downarrow)}{2R_\uparrow + 2R_\downarrow} = \frac{2R_\uparrow R_\downarrow}{R_\uparrow + R_\downarrow},$$

$$R_{AP} = \frac{R_\uparrow + R_\downarrow}{2},$$

where $R_\uparrow$ and $R_\downarrow$ are resistances of up spin and down spin current, respectively, and R_P and R_{AP} are total resistance of the SV having parallel and antiparallel alignment with the two FM electrodes, respectively.

In this model, although no consideration is given to the nonmagnetic layer between FM electrodes, the magnetoresistance (MR) ratio is commonly used to describe the difference between R_P and R_{AP} of the spin valve devices. The MR ratio is then given by

$$MR = \frac{R_{AP} - R_P}{R_P}.$$

1.2.2 Spin valve experiments

Typical characteristics of spin valve devices are shown in Fig. 1.2, where the device resistance is plotted as a function of the external magnetic field. With a high magnetic field, both FM electrodes are magnetized along the direction of the magnetic field. Since the alignment of the magnetization directions of the FM contact is parallel, the device resistance will be $\boldsymbol{R_P}$. Upon reaching a specific magnetic field, the alignment of the magnetization direction becomes antiparallel because of the difference between the coercive fields of the FM electrode ($\boldsymbol{H_{C1}}$ and $\boldsymbol{H_{C2}}$). The resistance of the spin valve device, $\boldsymbol{R_{AP}}$, is shown in Fig. 1.2. When the external magnetic field increases and exceeds the coercive field of the second FM contact $\boldsymbol{H_{C2}}$, the alignment of magnetizations becomes parallel again and the resistance returns to $\boldsymbol{R_P}$.

A peak is observed in the resistance between the coercive fields $\boldsymbol{H_{C1}}$ and $\boldsymbol{H_{C2}}$, as shown by the red curves in Fig. 1.2. When the magnetic field scans in the reverse direction, the same peak between the coercive fields is shown by the blue curve. If the total resistance of $\boldsymbol{R_{AP}}$ is smaller than that of $\boldsymbol{R_A}$, then a concave shape is produced instead of the peak.

1.2.3 Nonmagnetic layer in spin valve

So far, the discussion has focused only on the role of FM electrodes. The nonmagnetic layer and the interface between the FM electrodes and the nonmagnetic layer control the spin relaxation. The investigation of a spin transport and spin conserve medium is one of the more important topics in spintronics, leading to efficient manipulation of electron spins. To now consider spin transport and spin relaxation in the material, it is useful to define the spin diffusion length and the spin relaxation time. The spin diffusion length

indicates the distance at which electron spins can move in materials while conserving their own electron spin directions. The spin relaxation time is the time spent conserving the spin direction of electrons. More details will follow in the theoretical discussion in Chapter 3.

Recently, the materials researched seeking a new spin transport and conserving medium, have been extended to include not only metals but also semiconductors,[15] superconductors, [16] topological insulators, [17] carbon compounds, [18] organic semiconductors, polymers and organic conductors. Since the short spin relaxation time is on the order of picoseconds order, spintronics devices based on metals are not suitable for coherent spin manipulation.[18, 19] To increase the spin relaxation time in spintronic devices, hybrid devices with non-metal materials yield new possibilities for the future of spintronics.

1.3 Organic spintronics and its objectives

OMs have been expected to act as a new spin transport medium since OMs, consisting mainly of light atoms such as carbon, oxygen, and nitrogen, allow a low spin-orbit interaction (SOI), and a long spin relaxation time. For hydrogenic electrons resembling a wave function, the strength of the SOI is proportional to the fourth power of the atomic number. The transport from π-orbital electrons further suppresses the SOI.[20] Spin relaxation in OMs is relatively weak resulting in a spin relaxation time for OMs several orders of magnitude larger than that of metals.

In 2002, Dediu et al.[21] reported on an organic spin valve device using the organic semiconductor sexithenyl (T_6, Figure 1.3) thin film as a nonmagnetic spacer of the spin valves. The organic spin valve showed a change in resistance depending on the external

magnetic field. Even though the characteristics of their device is different from typical SV devices, and the device resistance is different before and after applying a magnetic field, it is the first demonstration of polarized spin transport through OMs. They varied the thickness of the organic layer from 100 nm to 500 nm, resulting in a resistance change only for 100–200 nm thickness. The spin diffusion length of T_6 at room temperature was estimated to be approximately 200 nm.

Two years after the demonstration by Dediu et al., Xiong et al.[22] observed clear spin valve characteristics based on the organic semiconductor 8-hydroxy-quinoline aluminum (Alq_3), shown in Figure 1.3. The resistance of the organic spin valve was shown to depend on the magnetization alignment of two FM electrodes. The device structure in their study has become the typical device structure of organic spin valves (OSVs), the so-called layered structure (Figure 1.4). The Jullière model was applied to their results, and the spin diffusion length of Alq_3 was estimated to be 45 nm at 11 K. The short spin diffusion length of Alq_3 was considered to have originated from the SOI enhanced by an aluminum element in the Alq_3 molecule. This spin diffusion length is similar to the length of a single-walled carbon nanotube estimated from the spin valve.[23]

Following these pioneering works, there have been many reports on organic spintronics. Chapter 2 will introduce developments that have improved the characteristics of OSV, such as enlarging the MR ratio and operating at room temperature, as well as the development of other spintronic devices such as the SV logic gate and the spin-polarized organic light emitting diode (OLED). Considering the background of organic spintronics should clarify the challenges and objectives in organic spintronics. There have been two main objectives in the field of organic spintronics. First, to better understand the spin transport in OMs by investigating the pure spin current from the evidence of electrical

spin injection and spin transport in OMs. Second, to understand what occurs at the interface between OMs and FMs since the interface will strongly influence the spin injection into OMs, resulting in the change in the characteristics of organic spintronic devices.

1.4 Objective of this study

The objective of this study is to investigate the spin injection and spin transport in OMs. The study is divided into two topics: i) the demonstration of electrical spin injection along with a discussion of spin transport and spin relaxation in OMs based on nonlocal spin valve measurements, and ii) the observation of large tunneling anisotropic magnetoresistance at the interface between FMs and OMs.

- **The nonlocal spin valve measurements**

One of the most representative methods for investigating spin injection and spin transport is to observe MR in the nonlocal spin valve structure. Although the nonlocal spin valve measurement has been well studied in the field of inorganic spintronics, it has yet to be demonstrated for OMs because of the difficulties in device fabrication. The nonlocal spin valves were prepared for this study by the use of single crystals of organic conductors and Au buffer layers between FMs and organic conductors. Spin diffusion length and spin relaxation time have been evaluated. The spin transport properties will be discussed based on spin relaxation rate in Chapter 4.

- **Tunneling anisotropic magnetoresistance (TAMR)**

The TAMR effect is an interface effect between the FM electrodes and the materials.

Although the TAMR effect is influenced by the interface magnetic anisotropy, TAMR has not been well investigated within the field of organic spintronics. A large TAMR effect is observed at the interface between the pentacene thin films and the LSMO prepared on a STO (110) substrate, suggesting that an active control of the interface may lead to an increase in interface magnetoresistance. Details of these results and discussions are described in Chapter 5.

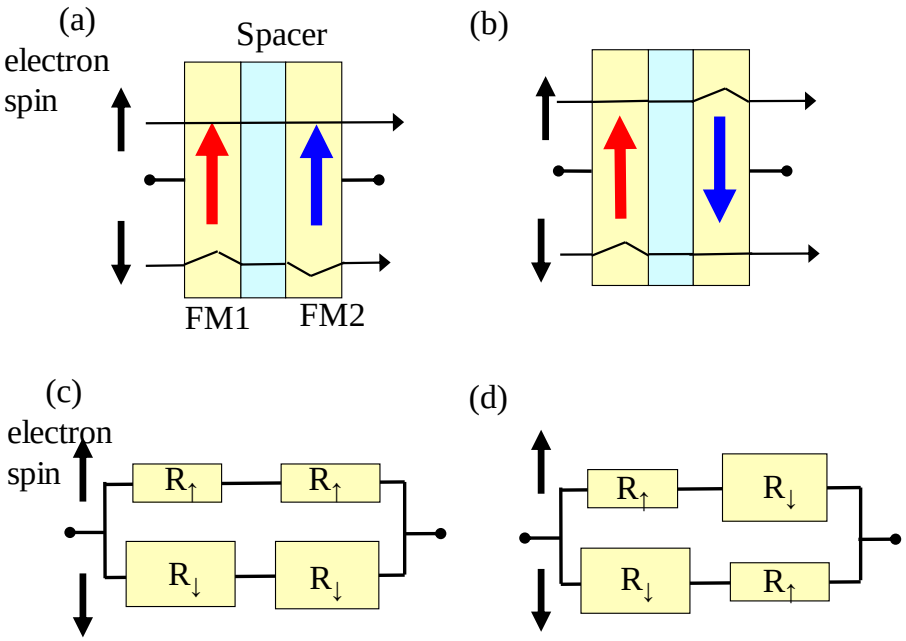

Figure 1: Schematic of a spin valve device with parallel (a) and antiparallel (b) configuration of magnetization direction of FM electrodes. Equivalent circuits for parallel and antiparallel configurations are given in (c) and (d), respectively. $R_{\uparrow}$ and $R_{\downarrow}$ denote the interface resistance at FM/spacer for upper and down spin electrons, respectively.

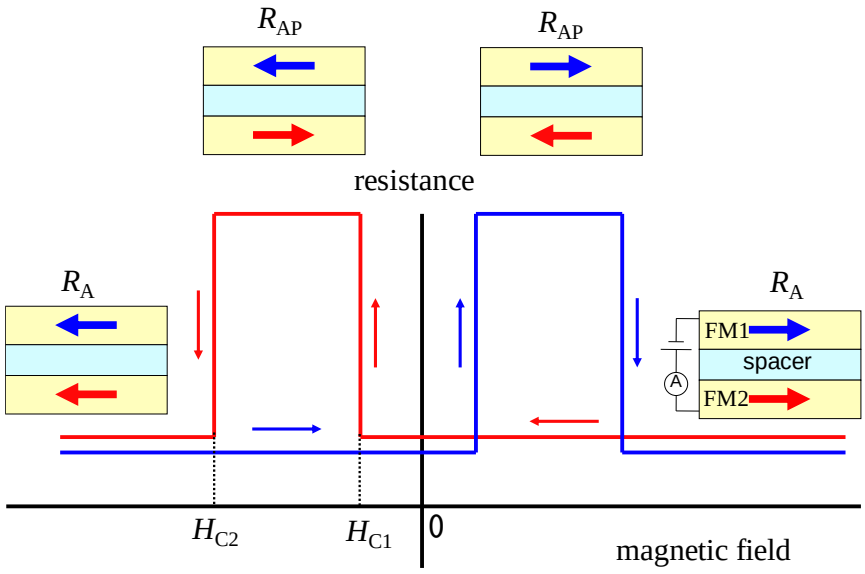

Figure 2: Plot of total resistance of a spin valve device as a function of the magnetic field. $\boldsymbol{H_{C1}}$ and $\boldsymbol{H_{C2}}$ denote the coercive field of FM electrode 1 and 2, respectively. The antiparallel configuration of the magnetization direction appears at the magnetic field between $\boldsymbol{H_{C1}}$ and $\boldsymbol{H_{C2}}$, showing high resistance of $\boldsymbol{R_{AP}}$. A parallel configuration with a low resistance of $\boldsymbol{R_A}$ is achieved at a magnetic field larger than $\boldsymbol{H_{C2}}$.

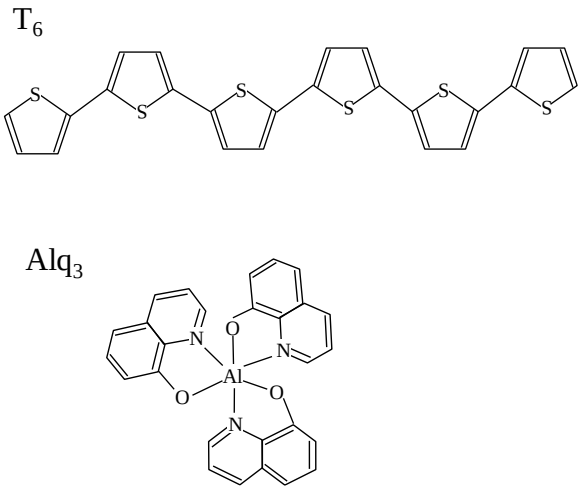

Figure 3: Molecular structures of T_6 and Alq_3.

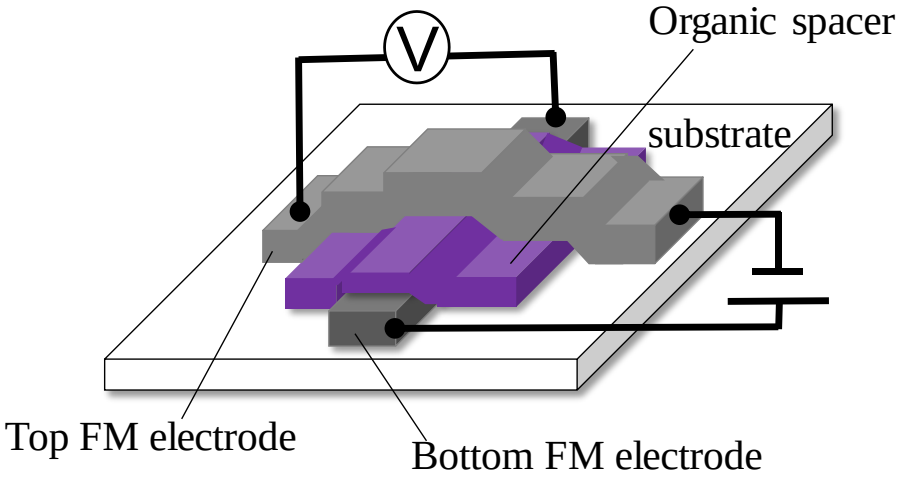

Figure 4. Schematic of typical organic spin valve devices, in which organic layer is sandwiched between two ferromagnetic electrodes.

Chapter 2

Background of the spin valve devices in organic spintronics

This chapter will introduce the background of the spin valve devices in organic spintronics. The main focus of organic spin valves (OSVs) has been to realize large MR at room temperature (RT) (See section 2.1). The research on OSVs is developing a better understanding of the interface between OMs and FM electrodes, and clarifying the spin transport behaviors in OMs that have become important to producing a large MR (See section 2.2). Although there have been some reports on spin valves based on OMs, the spin injection and spin transport remain unclear (See section 2.3). The nonlocal spin valve measurement is essential to the electrical spin injection and spin transport in the material (See section 2.3). Recently, there has been increased interest in research on functional OSVs in organic spin valves (See section 2.1 and 2.4), which requires an understanding of the spin injection and spin transport in OMs.

2.1 Organic spin valves

Since the pioneering reports by Dediu et al.[21] and Xiong et al.,[22] there have been many efforts to use OMs in spintronic devices due to the OMs consisting of light atoms such as carbon, nitrogen and oxygen that have low spin-orbit interaction (SOI), resulting in long spin relaxation time. The studies on organic spin valves (OSVs) have focused on: i) realizing large GMR/TMR ratio at room temperature; ii) proving spin injection and spin transport in OMs experimentally; and iii) developing functional organic spintronic devices such as spin-polarized OLEDs,[24–27] all-organic based spin valves,[28, 29] and a

multi-state OSV.[30, 31]

2.2 Enhancement of GMR/TMR effect in layered OSVs

According to the Jullière's model, which includes spin scattering in the spacer layer in spin valve devices, the MR is described by the ratio

$$\frac{\Delta R}{R} = \frac{2P_1P_2e^{-d/\lambda_S}}{1-P_1P_2e^{-d/\lambda_S}},$$

where R is the resistance of the spin valve, P_1 is the effective spin polarization of the injection current from the first magnetic electrode, P_2 is effective spin polarization of the injection current into the second magnetic electrode, λ_s is the spin diffusion length of the nonmagnetic layer, and d is the thickness of the nonmagnetic layer. One idea to enhance the MR ratio would be to choose a magnetic electrode with a high spin polarization. Another possibility would be to choose an OM with a long spin diffusion length, λ_s. Note that the spin polarization inside the bulk is different from that at the surface/interface of the magnetic electrodes, where P_1 and P_2 depend on the spin polarization at the interface. Park et al. indicated that the surface magnetization of $La_{0.7}Sr_{0.3}MnO_3$ (LSMO) measured by spin-resolved photoemission spectroscopy (SPES) is lower than that in the bulk as measured by a superconductor quantum interference device (SQUID).[32] Barraud et al. described P_1 of the Co/Alq_3 interface as larger than that of Co itself.[33] Lin et al.[34] and Tran et al.[35] show that P_1 and P_2 are strongly dependent on the thickness of the OM layer by use of a conductivity mismatch, which causes an underestimation of the spin diffusion length of OMs (mentioned below), a common problem in the research of low conductive OMs. Also note the challenge in discussing spin injection and spin transport in OMs based on layered OSVs, since the

characteristics of the layered OSV is affected by the interface (spin injection) and spin diffusion length (spin transport), simultaneously.

2.2.1 Magnetoresistance at low temperature and RT

The GMR/TMR characteristics of an OSV with a clear hysteresis curve were observed only at low temperatures.[22] The absence of MR at RT is attributed to two possible reasons: i) the spin diffusion length in the organic molecule (Alq_3) decreased with increasing temperature, and ii) the spin polarization at the surface of the LSMO electrodes decreased with increasing temperature. Regarding the former, Xiong et al. measured the MR of OSVs using Fe instead of LSMO to prove the reduction of the spin diffusion length of Alq_3 at RT. This is because Fe and Co have much higher Curie temperatures and keep their magnetization at RT.[32, 36, 37] The observed MR decreased with increasing temperature, and disappeared at 90 K. According to the Jullière model, if the temperature dependence of P_1 and P_2 is weak, the temperature dependence of MR is attributed to the temperature dependence of the spin diffusion length of the organic spacer. Drew et al. demonstrated the temperature dependence of the spin diffusion length of Alq_3 by a direct measurement of the spin diffusion length, as well observing the spin diffusion length of Alq_3 by a low energy muon spin rotation (LE-μSR) technique, which was seen to decrease from approximately 30 nm at 10 K to 10 nm at 100 K.[38] However, there have been other reports which show MR characteristics and spin transport in Alq_3 at RT,[39, 40] supporting the possibility of spin transport in OMs at RT. In addition, Jiang et al. demonstrated temperature independence of spin transport in Alq_3 as a result of spin pumping.[41] To understanding the spin transport and the spin relaxation mechanism in OMs, it is necessary to fabricate OSVs with a large MR.

Molecules with a weak SOI and hyperfine interaction (HFI) are important to obtain long spin diffusion lengths since the spin relaxation in OMs are mainly caused by the SOI and the HFI in the OMs.[42–44] Nguyen et al. studied the isotope effect of Alq_3 and π-conjugate polymer (poly(dioctyloxy)phenyl vinylene (DOO-PPV)) on the spin valve measurement and found that the D-Alq_3 and D-DOO-PPV, which replaced all hydrogen atoms (nuclear spin $I_H = 1/2$) with deuterium atoms (nuclear spin $I_D = 1$), showed a weaker HFI and larger MR than those of Alq_3 and DDO-PPV.[45, 46] They also found that the spin diffusion lengths of D-Alq3 and D-DOO-PPV were larger than those of Alq_3 and DDO-PPV on the basis of the organic layer thickness dependence of the MR. In 2011, Gobbi et al. used C_{60} molecule for OSVs. The HFI of the C_{60} molecule is very small since C_{60} has no hydrogen atoms and the nuclear spin of ^{12}C is zero. They reported MRs of 5–10 % at RT. The theoretical study by Bobbert et al. and Yu indicated the spin transports in OMs are affected by HFI[42] and SOI.[43, 44] Recent studies by Sayani et al.[47], Li et al.[48] and Jiang et al.[49] reported that the crystallinity and morphology of organic thin films and mobility of OMs significantly influence the GMR characteristics. These studies have also described that it is important to understand the spin transport behaviors in OMs for increasing MR.

Xiong et al. measured the temperature dependence of the magnetization of LSMO by a magneto-optic Kerr effect (MOKE) and showed that the surface magnetization of LSMO almost vanished around RT, resulting in a very low P_1 and the disappearance of MR at RT.[22] These results have been supported by a more detailed investigation using SQUID and SPES techniques by Park et al.[32] However, Ruden and Smith suggested in 2004 that the effective spin polarization at the interface between the magnetic electrode and the molecule differs from that of the surface of the magnetic electrodes without

organic films, which is very important to the spin injection into OMs,[50] an idea also introduced by Majumdar et al. in 2006.[51] They prepared OSV structures consisting of LSMO/regioregular poly(3-hexylthiophene) (RRP3HT)/Co with and without monolayer of an organic insulator such as hexamethyldisilazane (HMDS) on the LSMO electrode, and demonstrated that the device without the HMDS insulator layer shows a larger MR ratio at low temperature than that with HMDS. They also observed 1.5 % of the MR at RT despite using LSMO electrodes. Magnetic electrodes with high spin polarization at RT are also important. In 2013, Zhang et al.[52] demonstrated large MR ratio (5.3 %) at RT by using a Fe_3O_4 electrode that resulted in high spin polarization (80 %)[53] with high Curie temperature (860 K).[54] Kawasugi et al.[55] also obtained a large MR (7.8 %) at RT by using a half metal CMS[56] with high Curie temperature (985 K).[57] These studies indicate that controlling the spin polarization at the interface between the FM and the OMs is important in obtaining a large MR at RT.

As previously mentioned, there have been many reports on layered OSVs using various OMs since initially reported in 2004. Summarization of the MR ratios of OSVs reported so far are given in Table 1, together with the structures and experimental conditions. Moodera et al. realized a relatively high MR ratio of RT (4.6 % in 2007,[58] and 6.0 % in 2008[59]) using a very thin organic layer (<2 nm) as a tunneling barrier. In their experiments, the spin-polarized carriers are thought to be tunneling between two magnetic electrodes. In 2008, Vinzelberg et al. reported that the magnitude of MR and even the sign of MR in OSVs were changed because of the penetration of the magnetic metal particles from the top electrode into the organic layer. The thickness of this ill-defined layer was estimated to be 50–100 nm, which could form tunneling paths from the bottom magnetic electrode to the top magnetic electrode.[60, 61] Majumdar et al.[62] roughly

controlled the thickness of the ill-defined layer by changing the deposition rate of the top electrode and they observed a high TMR rate of 50–160 % at 5 K for the device with a thick ill-defined layer. In order to protect the organic layer from the penetration of the magnetic metal, some techniques have been demonstrated.[63] In 2010, Sun et al. introduced a buffer-layer assisted growth method (BLAG). Before evaporating the Co electrode onto the organic layer, they deposited a Co monolayer at low temperature.[63] With this technique, the penetration of Co particles into the organic layer was highly suppressed. They also observed a large MR ratio (~ 300 %) at 10 K for LSMO/Alq_3/Co layers. Barraud et al.[33] also observed a large TMR ratio (~ 300 % at 2 K) for a LSMO/Alq_3/Co structure by using the conductive AFM-tip technique. To explain the large MR ratio (300 %) observed by the two groups, the effective spin polarization at the Co/Alq_3 interface extracted from Jullière's formula for TMR ($\Delta R/R = 2P_1P_2/(1-P_1P_2)$) should be approximately 60 %,[33] which is much larger than that of the Co itself (34 %),[64] which suggests the existence of a new interface state between the molecules and the electrode that enhances the spin polarization, a so-called "spin-dependent hybridization" or "spinterface". This interface effect originates from a spin dependent broadening of the density of states.[33, 65] Optimizing the fabrication process of the OSVs has also clarified the importance of manipulating spin injection into OMs for increasing the GMR/TMR.

In summary, it is important to investigate the spin injection and the spin transport in OMs to increase the MR ratio at RT. However, the research of spin transport properties of OMs has been complex and unclear, as will be discussed in the following section (Section 2.3).

2.3 Spin injection and spin transport in OMs

A fundamental question to the organic spintronics is "Are the spin carriers really injected into the OMs and receive spin transport there?". Since the pioneering reports in 2002 and in 2004, much effort has been made to prove the spin injection from FM electrodes into OMs. The reasons given for the spin injection into OMs not being realized are: i) the MRs observed in previous studies originated from the TMR, where spin carriers are injected not into OMs but into another FM electrode via a direct tunneling process,[66, 67] and ii) there are interfacial effects such as tunneling anisotropic magnetoresistance (TAMR)[68, 69] and the interface MR,[70] indicating characteristics similar to the GMR effect. These factors complicate the discussion about the spin injection and spin transport in OMs.

2.3.1 TMR and GMR in OMs

In order to discuss whether spin injection into OMs is realized or not, it is important to clarify the carrier transport behaviors of OSVs. When direct tunneling occurs in OSVs, the spin injection and spin transport in OMs is not realized since the observed MR originates from the TMR effect. When the carrier injection/transport in OMs has occurred, the observed MR has originated from the GMR effect, which is affected not only by the effective injection/detection spin polarization at the interface, but also by the spin diffusion length and spin relaxation time of OMs. Thus, the properties of the OMs in the spin transport/conserve mediums would predict an efficient molecular design for future spintronic devices such as spin-polarized OLED,[24–27] spin-charge converter[41, 71, 72] and OSVs without FM electrodes.[28, 29] In order to simplify the following discussion, the interface effects of TAMR[68] and the interface MR[70] are not considered.

The strategy used to distinguish the tunneling and spin injection into OMs is to vary the thickness of the organic layer, then investigate the current-voltage (IV) characteristics of the OSV.[73, 74] In some studies, an insulating layer such as AlO_x was inserted between the organic layer and the top electrode to avoid the formation of an ill-defined layer.[61] The use of these techniques enables one to investigate the thickness dependence of the IV characteristics of the device to a thickness less than 10 nm.[75] Another option used to distinguish between charge tunneling and charge injection is to measure the temperature dependence of the conductance, observing the nonlinearity and parabolic behavior of the conductance versus junction voltage.[76]

To prove the spin injection into OMs directly, some groups have used other experimental approaches with nonelectrical techniques. In 2009, Cinchetti et al.[77] developed microscopic techniques, involving "two-photon photoemission," and Drew et al.[38] examined OMs using "low energy muon spin rotation" (LE-μSR) for evidence of spin injection. In the two-photon photoemission measurement, they prepared a Co/CuPc heterojunction and irradiated two successive laser pulses on the heterojunction. The first pulse generated the spin polarized electrons on the Co film, which would diffuse into the CuPc film. The second pulse excited the spin polarized electrons in the CuPc, resulting in photoemission. By measuring the spin direction and the energy of the photoemitted electrons, they obtained information about the spin-polarized electrons diffused into the CuPc film from the Co film.[77] The estimated efficiency of the spin injection from the Co film into the unoccupied molecular orbitals of CuPc was 85 %–90 %. Drew et al.[38] demonstrated the spin injection and the spin transport in the Alq_3 layer from the LE-μSR measurement. The prepared OSV consisted of NiFe/LiF/Alq_3/TPD/FeCo layers irradiated by muons with 100 % spin polarization to the OSV from the NiFe electrode side. The

muons penetrated Alq_3 layer and lost their energy, stopping at a penetration depth in Alq_3. The muons resulted in a spin-precession depending on the local magnetic field in Alq_3 layer before decaying into two neutrinos and a positron. The emission direction of them depends upon the spin direction of the muons at the time of the decay. The local magnetic field in the Alq_3 was correlated to the spin accumulation in Alq_3 layer, which depended on the distance from the NiFe electrodes. An estimate of the spin diffusion length for Alq_3 (30 nm at 10 K, and 10 nm at 90 K) was indicated by changing the irradiation energy of the muon.[38]

In 2013 and in 2014, Ando et al. demonstrated ferromagnetic resonance spin pumping[71, 72] in organic polymers (PEDOT:PSS and PBTTT) at room temperature. For their measurements, an organic-ferromagnetic material bilayer sample was placed under a magnetic field, a resonance field was applied to the sample, and voltages were measured as a function of the difference between the magnetic field and the resonance field. The magnetization precession excited by the magnetic field and the resonance field, is known as ferromagnetic resonance. Due to the strong spin-exchange coupling at the interface of OMs and FMs,[65] the spin injection into an OM occurred by exciting the magnetization precession in an adjacent ferromagnetic material, which then generates a pure spin current in the OMs (pure spin current is the flow of the electron spins without the flow of charge carriers). Based on the inverse spin Hall effect[6] (ISHE mechanism), since the spin current generates an electric field perpendicular to the spin current, the voltage peak depends on the difference between the magnetic field and the resonance field and is detected as proof of spin injection and spin transport in OMs. Following the studies of Ando et al., Jian et al. reported the spin pumping into Alq_3 and showed the temperature independence of spin diffusion lengths for Alq_3, which implied a spin relaxation was not caused by the SOI and

HFI.[41] Spin transport is shown to be dominated by the strong exchange coupling between localized carriers, like spin-wave spin current transport in magnetic insulators recently suggested by Yu.[78, 79] However, Sun et al.[80] studied the spin diffusion length of π-conjugated polymers containing intrachain Pt atoms with various concentrations. The SOI of the polymers depends on the concentrations of Pt atoms. The measured spin-diffusion lengths by a spin pumping increase with decreasing concentrations of Pt atoms, indicating the SOI dependence on the spin diffusion length.

Thus, the spin injection into OMs has been demonstrated, and investigations of the spin transport in OMs based on layered OSVs encouraged by the reports on microscopic techniques by Cinchetti et al.[77] and Drew et al.[38] in 2009.

2.3.2 Spin diffusion length in OMs

In the field of spintronics, the spin diffusion lengths and spin relaxation times are important parameters used in the design of spintronic devices. According to Jullère's formula for the GMR (Eq. 2.1), since the magnitude of the GMR decays exponentially with increasing thickness of the organic layer, one should be able to estimate the spin diffusion length by plotting the GMR effect as a function of the thickness of the organic layer. There have been reports that have estimated the spin diffusion length from the thickness of the organic layer dependence on the GMR.[45, 47–49, 76, 81]

In 2013, Zhang et al. reported that the GMR effect on OSVs consisting of Fe_3O_4/AlOx/C_{60}/Co layers increased with increasing thickness of the C_{60} layer, ranging from 10 nm to 80 nm.[52] They attributed this to the change in spin diffusion length depending on the thickness of the C_{60} layer, based on the theory suggested by Bobbert et al.[42] Lin et al. reported that the effective spin polarization at the interface decreases with

increasing thickness of the organic layer.[34] In 2012, Tran et al. discussed the correlation between the thickness of the organic layer and the conductivity mismatch by using a multistep tunneling model. In their model, charge carriers are transported by the tunneling process through localized intermediate states (Gaussian DOS of intermediate states), such as found in organic semiconductors.[35] This correlation between the conductivity mismatch and the thickness of the organic layer strongly affected the MR, irrespective of the spin lifetime and spin diffusion length of the organic film. These results indicate great complexity in describing the spin transport based on the organic layer thickness dependence of GMR in layered OSVs.

2.3.3 Pure spin current and nonlocal spin valve in OMs

The difficulties in discussing spin transport based on layered OSVs are caused by a charge current that flows with a spin current in OSVs. The change of the spin diffusion length depends on the electric field between the FM electrodes.[82] Spurious effects such as the anisotropic magnetoresistance (AMR),[83] the interface MR[35, 68–70] and the organic magnetoresistance (OMAR)[84] are in response to the charge current depending on the magnetization of the FM electrodes, or depending on the external magnetic field. Using the pure spin current in the represented methods avoids these difficulties. The spin pumping[71, 72] approach is used for investigating spin injection and spin transport in OMs. With this technique, the electric field generated by pure spin current via ISHE is measured, and the results of the carrier flow and accumulation. The possibility of spurious effects from the inorganic materials is still present since the spin pumping device structures are also layered structures.[71, 72] Sun et al.[80] reported that the spin diffusion length of C_{60} estimated by spin pumping was two orders of magnitude smaller than that of the

theoretical value[44] and experimental values from OSVs.[52]

It has been well documented that the most convincing evidence for the spin transport in materials is observed in the Hanle effect,[85–87] where a spin precession of electrons is caused by the magnetic field perpendicular to the direction of the electron spin. When the observed spin signal depends on the direction of the electron spin, the Hanle effect induces the oscillation of detected signals depending on the perpendicular magnetic field. The Hanle effect in OMs is detected using the spin pumping technique, but the observation of the Hanle effect using spin pumping is still controversial.[72] Other ways to observe Hanle effect using layered OSVs have been reported by Riminucci et al.[88] and Grünewald et al.[69] in 2013. Both groups observed no Hanle signal despite observing MR effects in OSVs. Riminucci et al. suggested that organic semiconductors must have high mobility to observe the Hanle effect,[88] and Grünewald et al. concluded that the observed MR in their experiment is not GMR but TMR.[69] Yu proposed a new spin transport mechanism in the OSCs that would suppress the Hanle effect by using a strong exchange coupling of the high density localized carriers in impurity band to transport the spin in OMs.[78, 79, 85] According to his discussion, the mobility of the spin (wave) current is much larger than that of the charge current(carrier). These results suggest that the field of organic spintronics requires more research to clarify the spin injection and spin transport in OMs.

An important subject of organic spintronics is the preparation of nonlocal spin valves.[87, 89, 90] The nonlocal spin valve measurement has been well studied in the field of inorganic spintronics since demonstrated by Jedema et al.[89] in 2001. The schematic of the nonlocal spin valve is shown in Figure 2.1, where the voltage probe and the current probe are in different circuits. The applied electric filed on the left two electrodes induces

the charge current flow toward the FM1 electrode. Since carriers injected from the FM2 electrode are spin polarized, a difference in the density of up spin electrons and down spin electrons appears in the nonmagnetic sample, thereby generating a density gradient of up spin and down spin electrons. Due to the density gradient of electron spins, the up spin and down spin are diffused in opposite directions to each other, as shown in Fig 2.1(b). This spin diffusion originates from the pure spin current that is detected as a voltage by the FM3 electrode. Similar to the effects of GMR/TMR, the detected voltage depends on the alignment between the magnetization direction of FM2 and FM3, referred to as the nonlocal magnetoresistance. The nonlocal spin valve measurements can detect the intrinsic spin signals injected from the FM2 electrode into the material without spurious signals from the charge current since the charge current path is completely separated from the spin current path.

Results of investigating the nonlocal spin valve measurements have been well documented for metals,[87, 89, 91] inorganic semiconductors,[92–94] and graphene,[95–98] allowing the analysis of the electrical spin injection, spin transport and spin relaxation mechanisms in such materials. However, the nonlocal MR has yet to be achieved in organic spintronics, although some groups have made significant efforts towards demonstrating the nonlocal MR.[99–101] Several reports are based on the lateral spin valve structure due to technological difficulties in the device fabrication process, indicating the challenges in realizing NLMR in organic spintronics.

2.4 Functional OSVs and the spinterface

One application of OSVs is the spin-polarized OLED (SP-OLED), that controls the intensity of electro luminescence by manipulating electron and hole spins.[24–27] The SP-

OLED consists of two FM electrodes, the emitting layer, the hole-transport layer and the electron-transport layer. In the absence of spin-polarization of excitons, the ratio between the singlet and triplet excitons is 1:3. If carriers in the emitting organic layer from the two FM electrodes are completely spin-polarized, and the FM electrodes are aligned in parallel, the spin of the electrons and holes generate singlet and triplet states with a 0:4 ratio in the emitting layer and the lack of singlet excitons in the emitting layer results in zero recombination efficiency. However, when the FM electrodes are aligned antiparallel, the electrons and holes generate singlet and triplet states with a ratio of 2:2, so that the internal quantum efficiency increases to 50 %. A basic concept of SP-OLED is realizing magnetic manipulation of the electro-luminescence. In 2004, Salis et al. demonstrated that the OLED device yields electro-luminescence (EL) results with hysteresis characteristics determined by the magnetization direction of the FM electrodes.[25] However, they concluded that the obtained hysteresis characteristics of the EL is not evidence of the spin injection, but instead a result of the magnetic field dependence of the EL intensity combined with stray magnetic fields from the electrodes. There are few investigation of the SP-OLED,[24–27] since many issues remain unsolved. The main difficulties in realizing the SP-OLED mentioned by Deckota et al.[90] are: i) to observe the EL requires the applied voltage to be larger than the band gap of the OMs although the spin polarization is greatly suppressed by the high voltage, as was reported by many groups; ii) the use of an interlayer at the interface (such as LiF) to manipulate the interfacial work function for the electron and hole injection/transport would substantially reduce the effective spin polarization at the interface between the FM electrode and the OMs, and iii) the magnetic field could change the formation of the singlet and the triplet excitons that causes OMAR effects in the bipolar region, complicating the mechanism of

the SP-OLED.

Research on a functional OSV device reported by Prezioso et al. in 2011, examines an integration of the memristor effect and the spin vale effect.[30] They demonstrate that the OSV consisting of LSMO/Alq_3/AlOx/Co layers showed an electrical hysteresis in IV characteristics when a high negative/positive bias voltage is applied, and that the GMR effect of their device could be changed by applying a pulse bias voltage. By using these properties of the spin valve device, three stable resistivity states of the spin valve could be freely switched. In 2012, the same group succeeded in fabricating a universal implication logic gate based on one single device. They also presented 32 distinct states, operating a 5-bit memory.[31] There have been other reports about an all-OSV device, where the FM electrodes are replaced with molecular magnets, enabling one to avoid the conductivity mismatch. In 2010 and in 2011, the group of Epstein et al. demonstrated OSVs using a molecular magnet as the FM electrodes.[28, 29]

Interest has grown in the hybridization effect at the interface between metals and OMs since it can increase spin polarization at the interface.[33, 65, 70, 102] Bairagi et al. reported that Co thin films coated with C_{60} easily changed the axis of magnetization direction from in-plane to out-of-plane.[103] In 2015, Ma'Mari et al. further demonstrated that Cu thin films having a molecular C_{60} film showed ferromagnetic characteristics.[104] Djeghloul et al.[105] studied the change of spin polarization at the interface of various combinations of molecules and FMs using photoemission spectroscopy. Increasing spin polarization at the interface was observed for all the combinations in their study. Understanding spin injection and spin transport is required for further research on functional OSVs and the spinterface.

Table 2.1: MR ratio of OSVs.

Years	OMs	FMs	MR (%) @ T (K)
2004 [22]	Alq_3 (130 nm)	LSMO, Co	-40 @ 11 K
2005 [106]	Alq_3 (140 nm)	Fe, Co	5 @ 11 K, 0 @ 90 K
2006 [51]	RRP3HT (100 nm)	LSMO, Co	80 @ 5 K, 1.5 % @ R.T.
2007 [107]	CVB (100 nm)	LSMO, Co	18 @ 14 K, 0 @ R.T.
2007 [58]	Alq_3 (160 nm)	Co/Al_2O_3, NiFe	7.5 @ 4.2 K, 6 @ R.T.
2008 [59]	Ruburene (4–18 nm)	Fe, Co	16 @ 4.2 K, 6 @ R.T.
2008 [61]	Alq_3 (100–200 nm)	LSMO, Al_2O_3/Co	-11 @ 20 K, 0.15 @ R.T.
2009 [108]	Alq_3 (1 nm) (2 nm) (4 nm)	CoFeB/Al_2O_3, Co	11 @ R.T. 4 @ R.T. 2.5 @ R.T.
2010 [33]	Alq_3 (2 nm)	LSMO, Co (AFM tip)	300 @ 2 K
2010 [63]	Alq_3 (95 nm)	LSMO, Co (BLAG)	300 @ 10 K
2010 [28]	Alq_3 (5 nm)	LSMO/LAO, V(TCNE)x	2 @ 100 K
2011 [34]	C_{60} (40 nm)	LSMO, Co	9 @ 15 K, 1 @ 200K
2012 [35]	C_{60} (5–28 nm)	Co/AlO_x, NiFe	5‑10 @ R.T.
2012 [46]	Alq_3 (40 nm) D-Alq_3 (40 nm)	LSMO, Co LSMO, Co	-20 @ 10 K -60 @ 10 K
2013 [52]	C_{60} (80 nm)	Fe_3O_4/AlO_x, Co	6.9 @ 150 K, 5.3 @ R.T.
2013 [55]	TPD (200 nm)	CMS, Co	19 @ 5 K, 7.8 @ R.T.
2013 [47]	RRaP3HT (80 nm) RRP3HT(80 nm)	LSMO, Co LSMO, Co	23 @ 5 K 50 @ 5 K
2014 [109]	BCP (10 nm),	Flexible substrate Co/AlO_x, NiFe	3.5 @ R.T.
2014 [40]	Alq_3 (50 nm)	LSMO, Co (back deposition)	-20 @ 10 K, -2 @ R.T.
2015 [48]	P(NDI2OD-T2)	LSMO, AlO_x/Co	90 @ 4.2 K, 6.8 @ R.T.
2015 [81]	Alq_3 (50 nm), Irq_3 (50 nm)	LSMO, Co LSMO, Co	-8 @ 10 K -9 @ 10 K
2015 [110]	Rubrene (2–20 nm)	Fe_3O_4/AlO_x, Co	11 @ 150 K, 6 @ R.T.
2016 [111]	CoPc H2Pc/MnPc	Co, Co (AFM-tip)	More than 1,000 @ 2 K

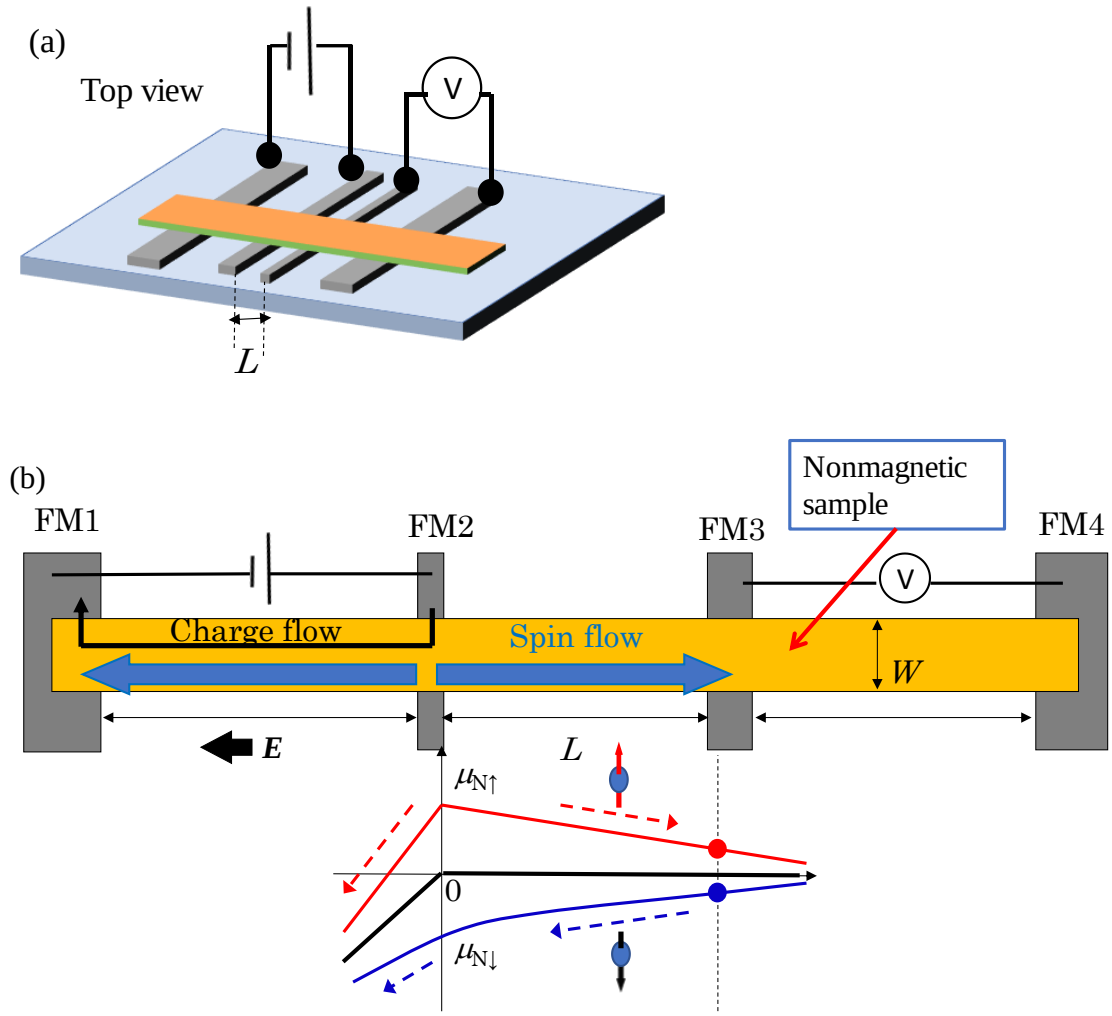

Figure 2.1: (a) Schematic of the nonlocal spin valve device. (b) The spin flow and charge flow in the nonlocal spin valves. The gradient of the electrochemical potential of the electron up spin (red) and the down spin (blue) is depicted, where the Y axis shows the electrochemical potential and the X axis shows the distance from FM 2 electrode. The black curve indicates the average value of the electrochemical potential of the up spin and down spin of electrons.

Chapter 3

Theoretical calculation of spin injection and spin transport

In this chapter, I show the theoretical calculation of electrical spin injection from FM electrode into nonmagnetic materials. Under the assumption of existence an insulating layer or a tunneling barrier between OMs and FMs, the calculation of the spin injection dealt in this chapter can be applied to OMs. This chapter also indicates theoretical explanation about the spin injection and the spin detection in nonlocal spin valve devices, which is used in chapter 4.

3.1 Electrical spin injection from FM electrodes into nonmagnetic materials

3.1.1 Electrochemical potential

It is important to introduce the electrochemical potential $\boldsymbol{\mu}$ which is useful to describe spin injection and spin transport in nonmagnetic materials. The charge current $\boldsymbol{J}^{charge}$ could be divided into up spin current $\boldsymbol{J}_{\uparrow}$ and down spin current $\boldsymbol{J}_{\downarrow}$ as described in chapter 1. The $\boldsymbol{J}^{charge}$ in materials also can be written with the drift term and the diffusion term characterized by the non-equilibrium electron density *grad(n_s)* as follows:

$$\begin{aligned} \boldsymbol{J}^{charge} = \boldsymbol{J}_{\uparrow} + \boldsymbol{J}_{\downarrow} &= \sum_{s=\uparrow,\downarrow} J_s^{drift} + J_s^{diffusion} \\ &= \sum_{s=\uparrow,\downarrow} \left(\sigma_s E + eD_s grad(n_s)\right) \\ &= \sum_{s=\uparrow,\downarrow} \left(-\sigma_s grad(\phi) + eD_s grad(n_s)\right), \end{aligned} \tag{3.1}$$

where σ_s, E, e, D_S, J_s^{drift}, and $J_s^{diffusion}$ are the conductivity of materials, the electric field, the elemental charge, the diffusion constant, and the drift term and the diffusion term of the current, respectively. $s = \uparrow, \downarrow$ shows the up/down spin state of the electron spins. According to the definition of chemical potential $\delta\mu_s \equiv \delta n_s / N_s$, and Einstein relation,

$$\sigma_s = e^2 N_s D_s, \tag{3.2}$$

where N_S is the density of state at the Fermi energy. One could describe Eq. (3.1), which depends on the state of the electron spin, into:

$$J_s = \sigma_s grad(\bar{\mu}_s)/e, \tag{3.3}$$

where $\bar{\boldsymbol{\mu}}$ is the electrochemical potential, $\bar{\mu} = \mu - e\phi$. By using the electrochemical potential, one could see that the carrier current $\boldsymbol{J}$ is described in Eq. (3.3), and indicates that $\boldsymbol{J}$ depends on the gradient of the electrochemical potential irrespective of the electric field. Therefore, I could summarize the equation of charge current $\boldsymbol{J}^{charge} = \boldsymbol{J}_\uparrow + \boldsymbol{J}_\downarrow$ and spin current $\boldsymbol{J}^{spin} = -\frac{\hbar}{2e}(\boldsymbol{J}_\uparrow - \boldsymbol{J}_\downarrow)$ described as

$$\boldsymbol{J}^{Charge} = \frac{\sigma_\uparrow}{e} grad(\bar{\mu}_\uparrow) + \frac{\sigma_\downarrow}{e} grad(\bar{\mu}_\downarrow), \tag{3.4}$$

$$\boldsymbol{J}^{spin} = -\frac{\hbar}{2e^2}\left(\sigma_\uparrow grad(\bar{\mu}_\uparrow) - \sigma_\downarrow grad(\bar{\mu}_\downarrow)\right), \tag{3.5}$$

where $\hbar$ is a reduced Planck constant. Particularly, in the nonmagnetic materials, since the conductivity of spin up electron and spin down electron is the same value, Eq. (3.5) could be described as

$$\boldsymbol{J}^{\boldsymbol{Charge}} = \frac{\sigma}{\boldsymbol{e}} \boldsymbol{grad}(\bar{\boldsymbol{\mu}}_\uparrow + \bar{\mu}_\downarrow), \tag{3.6}$$

$$\boldsymbol{J}^{\boldsymbol{spin}} = -\frac{\sigma\hbar}{\boldsymbol{2e^2}} \boldsymbol{grad}(\bar{\boldsymbol{\mu}}_\uparrow - \bar{\mu}_\downarrow), \tag{3.7}$$

Eq. (3.6) means that charge current derives from the average of electrochemical potential. When there is no charge accumulation or gradient, the charge current is determined by

the gradient of a voltage ϕ. On the other hand, Eq. (3.7) means that the spin current derives from the gradient of the difference between electrochemical potential of up spin electrons and down spin electrons $(\overline{\boldsymbol{\mu}_{\uparrow}} - \overline{\boldsymbol{\mu}_{\downarrow}})$. We could regard $(\overline{\boldsymbol{\mu}_{\uparrow}} - \overline{\boldsymbol{\mu}_{\downarrow}})$ as a voltage for the spin current.

3.1.2 Spin diffusion length and spin relaxation time

Before describing the spin injection into nonmagnetic materials from FM electrodes, it is important to introduce the spin diffusion length λ_{sf} and the spin relaxation time τ_{sf}. In the previous section, the characteristics of the spin current seems to resemble to that of the charge current. However, there is an absolute difference between the spin current and charge current. This is an existence of the conservation law. For the charge current, there is a charge conservation law derived from Maxwell's equations, which is the principle meaning that the electric charge neither be created nor be destroyed. The charge conservation law is described by

$$\frac{\partial \rho}{\partial t} + \nabla \cdot \boldsymbol{J} = 0, \tag{3.8}$$

where ρ is a charge density. Because the charge current is a conserved quantity, the same amount of the charge current in the conductive wire can be extracted from other end regardless of the length of a conducting wire, when the charge current flows from one end. On the other hand, a conservation low for the spin current is not exist. This means that it is difficult to flow the spin current over long distances because the spin current is not a conserved quantity. The electron spin flips its direction from up/down spin to down/up spin with a certain probability because of some spin relaxation mechanisms in materials such as SOI, resulting in $(\overline{\boldsymbol{\mu}_{\uparrow}} - \overline{\boldsymbol{\mu}_{\downarrow}}) = 0$. Therefore, the spin current disappears when it flows a certain distance or for a certain amount of time. This distance is called

the spin diffusion length and the time is called spin relaxation time.

Since the spin current is not a conserved quantity, the expression of the spin current is described as

$$\frac{\partial \rho_s}{\partial t} + \nabla \cdot \boldsymbol{J}_s = \boldsymbol{T}, \tag{3.9}$$

where ρ_s and $\boldsymbol{T}$ are a spin density and spin relaxation term which indicate the creation or the disappearance of the electron spin due to spin relaxation of electron spins. According to the reference [91, 112], $\boldsymbol{T}$ is described as

$$\boldsymbol{T} = -e\frac{\delta n_\uparrow}{\tau_{\uparrow\downarrow}} + e\frac{\delta n_\downarrow}{\tau_{\downarrow\uparrow}}, \tag{3.10}$$

where $\tau_{\uparrow\downarrow}$ and $\tau_{\downarrow\uparrow}$ are the spin scattering time from spin state up to down and from spin state down to up, respectively. At the steady state, since the number of up spin electrons and down spin electrons is unchanged, one can describe the equation as follows

$$\begin{aligned} 0 &= \frac{\delta n_\downarrow}{\tau_{\downarrow\uparrow}} - \frac{\delta n_\uparrow}{\tau_{\uparrow\downarrow}} - \frac{1}{e}\nabla j_\uparrow, \\ 0 &= \frac{\delta n_\uparrow}{\tau_{\uparrow\downarrow}} - \frac{\delta n_\downarrow}{\tau_{\downarrow\uparrow}} - \frac{1}{e}\nabla j_\downarrow, \end{aligned} \tag{3.11}$$

By using the relations $\delta n_s = N_s \delta \mu_s$, $\delta\mu_\uparrow - \delta\mu_\downarrow = \overline{\boldsymbol{\mu}_\uparrow} - \overline{\boldsymbol{\mu}_\downarrow}$, Eq. (3.1) and the detailed balancing $\frac{N_\uparrow}{\tau_{\uparrow\downarrow}} = \frac{N_\downarrow}{\tau_{\downarrow\uparrow}}$, one can obtain[112]

$$\nabla^2(\sigma_\uparrow \bar{\mu}_\uparrow + \sigma_\downarrow \bar{\mu}_\downarrow) = 0, \tag{3.12}$$

$$D'\nabla^2(\bar{\mu}_\uparrow - \bar{\mu}_\downarrow) = \frac{1}{\tau_{\mathrm{sf}}}(\bar{\mu}_\uparrow - \bar{\mu}_\downarrow), \tag{3.13}$$

with

$$D' = \frac{(N_\uparrow + N_\downarrow)D_\uparrow D_\downarrow}{N_\uparrow D_\uparrow + N_\downarrow D_\downarrow}, \tag{3.14}$$

$$\tau_{\mathrm{sf}} = 2\left(\frac{1}{\tau_{\downarrow\uparrow}} + \frac{1}{\tau_{\uparrow\downarrow}}\right)^{-1}, \tag{3.15}$$

One can obtain the general solution in one dimension of Eq. (3.13) with introducing the

spin dependent voltage $\Delta V_S \equiv \frac{\overline{\mu_\uparrow} - \overline{\mu_\downarrow}}{e} = \frac{\Delta\overline{\mu}}{e}$ and the general solution of Eq. (3.13) is described as

$$\Delta V_{\mathrm{S}} = V_{\mathrm{A}} \exp(-\frac{x}{\sqrt{D'\tau_{sf}}}) + V_{\mathrm{B}} \exp\left(\frac{x}{\sqrt{D'\tau_{sf}}}\right), \tag{3.16}$$

Eq. (3.16) indicate that ΔV_{S} is decaying with a certain value of $\sqrt{D'\tau_{sf}}$, which is the spin diffusion length λ_{sf} of the materials. The relationship between the spin diffusion length and the spin relaxation time is described as $\lambda_{\mathrm{sf}} = \sqrt{D'\tau_{\mathrm{sf}}}$.

3.1.3 The spin injection into nonmagnetic materials from FM electrodes

In this section, I consider the spin injection at the interface between nonmagnetic materials (NM) and FM. Based on the discussion in the previous sections, it is enables us to describe the electrochemical potential at the interface of NM/FM as shown in Figure 3.1 by using Eq. (3.6), Eq. (3.7), Eq. (3.12) and Eq. (3.13). It is described as a function of z follows:

FM

$$\overline{\mu_\uparrow}(z) = \frac{A}{\sigma_\uparrow} \exp\left(\frac{z}{\lambda_{\mathrm{F}}}\right) + Bz + C, \tag{3.17}$$

$$\overline{\mu_\downarrow}(z) = -\frac{A}{\sigma_\downarrow} \exp\left(\frac{z}{\lambda_{\mathrm{F}}}\right) + Bz + C, \tag{3.18}$$

NM

$$\overline{\mu_\uparrow}(z) = \frac{a}{\sigma} \exp\left(-\frac{z}{\lambda_{\mathrm{N}}}\right) + bz, \tag{3.19}$$

$$\overline{\mu_\downarrow}(z) = -\frac{a}{\sigma} \exp\left(-\frac{z}{\lambda_{\mathrm{N}}}\right) + bz, \tag{3.20}$$

where λ_{F}, λ_{N} are the spin diffusion length of the FM and the NM, respectively. *A*, *B*, *C*, *a*, and *b* are the constant determined by the boundary condition, and *z* is a coordinate. The interface between FM and NM is corresponding to $z = 0$. The continuity condition for the electrochemical potential and the boundary condition for the current at the interface

are described as

$$\bar{\mu_{\uparrow}} = \frac{A}{\sigma_{\uparrow}} + C = \frac{a}{\sigma}\ , \qquad \bar{\mu_{\downarrow}} = -\frac{A}{\sigma_{\downarrow}} + C = -\frac{a}{\sigma}\ , \tag{3.21}$$

$$eJ_{\uparrow} = \frac{A}{l_{\mathrm{F}}} + \sigma_{\uparrow}B = -\frac{a}{l_{\mathrm{N}}} + \sigma b, \qquad eJ_{\downarrow} = -\frac{A}{l_{\mathrm{F}}} + \sigma_{\downarrow}B = \frac{a}{l_{\mathrm{N}}} + \sigma b, \tag{3.22}$$

From Eqs. (3.17)–(3.22), one can obtain

$$\frac{J_{\uparrow} - J_{\downarrow}}{J_{\uparrow} + J_{\downarrow}} = \frac{\beta}{1 + {r_N}/{r_{\mathrm{F}}}}, \tag{3.23}$$

$$\beta = \frac{\sigma_{\uparrow} - \sigma_{\downarrow}}{\sigma_{\uparrow} + \sigma_{\downarrow}} = \frac{\sigma_{\uparrow} - \sigma_{\downarrow}}{\sigma}, \tag{3.24}$$

with

$$r_{\mathrm{N}} = \frac{l_{\mathrm{N}}}{2\sigma}, \tag{3.25}$$

$$r_{\mathrm{F}} = \frac{l_{\mathrm{F}}}{4}\left(\sigma_{\uparrow}^{-1} + \sigma_{\downarrow}^{-1}\right), \tag{3.26}$$

where r_N and r_F represent the resistance of NM and FM, respectively.[112] In Eq. (3.23), the efficiency of the spin injection decrease with increasing $r_{\mathrm{N}}/r_{\mathrm{F}}$, which is depending on the conductivity of NM and FM. This phenomenon is the conductivity mismatch. The conductivity mismatch tends to be a problem when we attempt to inject the spin polarized current into inorganic semiconductors or OMs because of their low conductivity. Takahashi and Maekawa reported that the conductivity mismatch could be avoid by introducing an insulating layer between NM and FM.[112] When the insulating layer is inserted at the interface between NM and FM, the continuity condition for the electrochemical potential is modified as

$$\bar{\mu}_{\uparrow} = \frac{A}{\sigma_{\uparrow}} + C + r_{i\uparrow}eJ_{\uparrow} = \frac{a}{\sigma}, \tag{3.27}$$

$$\bar{\mu}_{\downarrow} = -\frac{A}{\sigma_{\downarrow}} + C + r_{i\downarrow}eJ_{\downarrow} = -\frac{a}{\sigma}, \tag{3.28}$$

where r_i is an interface resistance. One can obtain the efficiency of the injection of spin

polarized current described as

$$\frac{J_\uparrow - J_\downarrow}{J_\uparrow + J_\downarrow} = \frac{r_F\beta + r_i\beta^{"}}{r_F + r_N + r_i}, \tag{3.29}$$

$$\beta^{"} = \frac{{r_{i\uparrow}}^{-1} - {r_{i\downarrow}}^{-1}}{{r_{i\uparrow}}^{-1} + {r_{i\downarrow}}^{-1}}, \tag{3.30}$$

Eq. (3.29) and Eq. (3.30) indicate that the large r_i can realize the high efficiency of the spin injection even if the resistance of NM is high.[112]

3.2 The spin injection and the spin detection in the nonlocal spin valves

In this section, I introduce the spin injection and the spin detection in the nonlocal spin valve devices. Figures 2.1 indicate the schematic of the nonlocal spin valve device and the electrochemical potential of us spin electrons and down spin electrons in NM. As described in section 2.3.4, the nonlocal spin valve devices can detect the pure spin current in NM since the spin current path is separated from the charge current path as shown in Figs. 2.1. When the length between FM2 and FM3 in Figure 2.1 is shorter than the spin diffusion length of NM, the difference between the electrochemical potential of up spin electrons and down spin electrons $(\Delta\bar{\mu} = \bar{\mu_\uparrow} - \bar{\mu_\downarrow})$ does not equal zero at the interface between NM and detecting FM3 electrodes in Fig 2.1. Therefore, the pure spin current described as Eq. (3.7) is injected into FM3 electrodes. The spin relaxation of injected pure spin current into FM depends on the spin diffusion length of FM electrode. Since the spin diffusion length of FM electrodes is generally small (several nano meters),[91] $\Delta\bar{\mu}$ immediately becomes zero as shown in Figures 3.1. The density of state of up spin electrons and down spin electrons in FM electrodes depends on the magnetization direction of FM3 electrode. The spin direction of pure spin current also depends on the magnetization direction of injection FM2 electrodes. When the alignment of these two

FM electrodes is parallel, a positive bias ($V_{\mathrm{P}} = \bar{\mu}/e$) is detected. When alignment of these two FM electrodes is antiparallel, a negative bias ($V_{\mathrm{AP}} = -\bar{\mu}/e$) is detected as shown in Figures 3.1. In the measurement of nonlocal spin valve devices, the difference of the voltages $\Delta V_{\mathrm{s}} = V_{\mathrm{P}} - V_{\mathrm{AP}}$ is used to avoid the background of the detected voltage. Generally, since the detected voltage is proportional to the amount of the injection current from FM2 electrodes $\boldsymbol{I}_{\mathrm{inj}}$, the normalized value $\Delta R_{\mathrm{s}} \equiv \Delta V_{\mathrm{s}}/I_{\mathrm{inj}}$ is also used.

Next, I would like to estimate the value of the detected voltage normalized by $\Delta V_{\mathrm{s}}/I_{\mathrm{inj}}$. To describe the electrochemical potential in injection FM1 electrodes, NM and detected FM2 electrodes, I set the x axis and z axis in the nonlocal spin valve device as shown in Figure 3.2. In this calculation of detected voltage, I assume the condition that FM1 and FM2 are the same ferromagnetic material and the FM1/NM junction and NM/FM2 junction are the Ohmic contact. The electrochemical potentials in the FM1 ($z < 0$), the NM ($0 < z < \mathrm{L}, 0 < x < \mathrm{L}, \mathrm{L} < x$), and FM2 ($\mathrm{L} < z$) are described, respectively, as

$z < 0$

$$\bar{\mu_{\uparrow}} = \frac{A}{\sigma_{\uparrow}} \exp\left(\frac{z}{l_{\mathrm{F}}}\right) + Bz + C, \tag{3.31}$$

$$\bar{\mu_{\downarrow}} = -\frac{A}{\sigma_{\downarrow}} \exp\left(\frac{z}{l_{\mathrm{F}}}\right) + Bz + C, \tag{3.32}$$

$z > 0$

$$\bar{\mu_{\uparrow}} = \frac{a_z}{\sigma} \exp\left(-\frac{z}{l_{\mathrm{N}}}\right) + bz, \tag{3.33}$$

$$\bar{\mu_{\downarrow}} = -\frac{a_z}{\sigma} \exp\left(-\frac{z}{l_{\mathrm{N}}}\right) + bz, \tag{3.34}$$

$0 < x < \mathrm{L}$

$$\bar{\mu_{\uparrow}} = \frac{a}{\sigma} \exp\left(-\frac{x}{l_{\mathrm{N}}}\right) + \frac{c}{\sigma} \exp\left(\frac{x}{l_{\mathrm{N}}}\right), \tag{3.35}$$

$$\bar{\mu_{\downarrow}} = -\frac{a}{\sigma} \exp\left(-\frac{x}{l_{\mathrm{N}}}\right) - \frac{c}{\sigma} \exp\left(\frac{x}{l_{\mathrm{N}}}\right), \tag{3.36}$$

$z > \mathrm{L}$

$$\bar{\mu_{\uparrow}} = \frac{F}{\sigma_{\uparrow}} \exp\left(-\frac{(z-L)}{l_{\mathrm{F}}}\right) + G, \tag{3.37}$$

$$\tag{3.38}$$

$$\bar{\mu_{\downarrow}} = -\frac{F}{\sigma_{\downarrow}}\exp\left(-\frac{(z-L)}{l_{\mathrm{F}}}\right) + G,$$

$$\bar{\mu_{\uparrow}} = \frac{f}{\sigma}exp\left(-\frac{(x-L)}{l_{\mathrm{N}}}\right), \tag{3.39}$$

$x >$ L

$$\bar{\mu_{\downarrow}} = -\frac{f}{\sigma}exp\left(-\frac{(x-L)}{l_{\mathrm{N}}}\right), \tag{3.40}$$

where $A, B, C, a_z, a, b, c, F, G, f$ are the constant, and l_{F} and l_{N} are the spin diffusion length of the FM and the NM, respectively. Especially, the value of G divided by the charge element indicates detected voltage $V_{\mathrm{s}} = G/e$.

The continuity condition for the electrochemical potentials and the boundary condition for the current at the $z = 0$ and the $x = 0$ are described, respectively, as

$$\bar{\mu_{\uparrow}} = \frac{A}{\sigma_{\uparrow}} + C = \frac{a_z}{\sigma} = \frac{a+c}{\sigma}, \tag{3.41}$$

$$e\bar{\mu_{\downarrow}} = -\frac{A}{\sigma_{\downarrow}} + C = -\frac{a_z}{\sigma} = -\frac{a+c}{\sigma}, \tag{3.42}$$

$$eJ_{\uparrow} = \frac{A}{l_{\mathrm{F}}} + \sigma_{\uparrow}B = -\frac{a+a_z-c}{l_{\mathrm{N}}} + \sigma b, \tag{3.43}$$

$$eJ_{\downarrow} = -\frac{A}{l_{\mathrm{F}}} + \sigma_{\downarrow}B = \frac{a+a_z-c}{l_{\mathrm{N}}} + \sigma b, \tag{3.44}$$

I can obtain the Equation (3.45) by Eqs. (3.41)–(3.44) and Eq. (3.24), which is described as

$$4l_{\mathrm{F}}^{-1}\frac{\sigma^{-1}}{\sigma_{\uparrow}^{-1}+\sigma_{\downarrow}^{-1}}a + 4l_{\mathrm{N}}^{-1}a + 4l_{\mathrm{F}}^{-1}\frac{\sigma^{-1}}{\sigma_{\uparrow}^{-1}+\sigma_{\downarrow}^{-1}}c = -e\beta J. \tag{3.45}$$

The equation (3.46) is also described by using Eq. (3.25) and Eq. (3.26)

$$(r_N + 2r_F)a + r_N c = -r_N r_F \sigma e\beta J. \tag{3.46}$$

In the same way, he continuity condition for the electrochemical potentials and the boundary condition for the current at the $z = L$ and the $x = L$ are described, respectively, as

$$\bar{\mu_{\uparrow}} = a\sigma^{-1}\eta + c\sigma^{-1}\eta^{-1} = \sigma_{\uparrow}^{-1}F + G = \sigma^{-1}f, \tag{3.47}$$

$$\bar{\mu_{\downarrow}} = -a\sigma^{-1}\eta - c\sigma^{-1}\eta^{-1} = -\sigma_{\downarrow}^{-1}F + G = -\sigma^{-1}f, \tag{3.48}$$

$$eJ_{\uparrow} = -l_{\mathrm{N}}^{-1}(a\eta - c\eta^{-1}) = -l_{\mathrm{F}}^{-1}F - l_{\mathrm{N}}^{-1}f, \tag{3.49}$$

$$eJ_{\downarrow} = l_{\mathrm{N}}^{-1}(a\eta - c\eta^{-1}) = l_{\mathrm{F}}^{-1}F + l_{\mathrm{N}}^{-1}f, \tag{3.50}$$

$$\eta = \exp(-L/l_{\mathrm{N}}), \tag{3.51}$$

By the use of Eqs. (3.47)–(3.51), I can obtain the Equations (3.52)–(3.53) described as

$$F = -2l_{\mathrm{N}}^{-1}l_{\mathrm{F}}\eta^{-1}c, \qquad G = -2r_{\mathrm{F}}\beta' l_{\mathrm{F}}^{-1}F, \tag{3.52}$$

$$\beta' = \frac{\sigma_{\uparrow}^{-1} - \sigma_{\downarrow}^{-1}}{\sigma_{\uparrow}^{-1} + \sigma_{\downarrow}^{-1}}, \tag{3.53}$$

$$r_{\mathrm{N}}\eta a + (r_{\mathrm{N}} + 2r_{\mathrm{F}})\eta^{-1}c = 0, \tag{3.54}$$

From the simultaneous equation between Eq. (3.46) and Eq. (3.54), I can obtain Equation (3.55) described as

$$\begin{pmatrix} a \\ c \end{pmatrix} = -\frac{r_{\mathrm{N}}r_{\mathrm{F}}\sigma e\beta J}{(r_{\mathrm{N}} + 2r_{\mathrm{F}})^2\eta^{-1} - r_{\mathrm{N}}^2\eta}\begin{pmatrix} (r_{\mathrm{N}} + 2r_{\mathrm{F}})\eta^{-1} \\ -r_{\mathrm{N}}\eta \end{pmatrix}. \tag{3.55}$$

The spin signal in nonlocal spin valve device $V_{\mathrm{s}} = G/e$ is obtained by substituting Eq. (3.55) into Eq. (3.52), which is described as

$$\frac{G}{eJ} = R_s = \frac{2\left({}^{r_{\mathrm{F}}}/_{r_{\mathrm{N}}}\right)^2 r_{\mathrm{N}}\beta^2}{\left(1 + 2\,{}^{r_{\mathrm{F}}}/_{r_{\mathrm{N}}}\right)^2 - \eta^2}\eta, \tag{3.56}$$

According to the previous report by Takahashi and Maekawa,[112] the spin signal in nonlocal spin valve measurement including interface resistance is described as

$$\begin{aligned} V_{\mathrm{s}}/I = \pm 2R_{\mathrm{N}}e^{-L/\lambda_{\mathrm{N}}}\prod_{i=1}^{2}\left(\frac{P_{\mathrm{J}}\frac{R_i}{R_{\mathrm{N}}}}{1 - P_{\mathrm{J}}^2} + \frac{p_{\mathrm{F}}\frac{R_{\mathrm{F}}}{R_{\mathrm{N}}}}{1 - p_{\mathrm{F}}^2}\right) \\ \times\left[\prod_{i=1}^{2}\left(\frac{2\frac{R_i}{R_{\mathrm{N}}}}{1 - P_{\mathrm{J}}^2} + \frac{2\frac{R_{\mathrm{F}}}{R_{\mathrm{N}}}}{1 - p_{\mathrm{F}}^2}\right) - e^{-2L/\lambda_{\mathrm{N}}}\right]^{-1}, \end{aligned} \tag{3.57}$$

where signs "+" and "−" correspond to the parallel and antiparallel alignments of FM electrodes, respectively, $R_{\mathrm{N}} = \rho_{\mathrm{N}}\lambda_{\mathrm{N}}/A_{\mathrm{N}}$ and $R_{\mathrm{F}} = \rho_{\mathrm{F}}\lambda_{\mathrm{F}}/A_{\mathrm{F}}$ are the resistances of NM and FM with the cross sections area A_{N} and A_{F} and the spin diffusion lengths of NM λ_{N} and that of FM λ_{F}, respectively. p_{F} is the spin polarization of FM. The spin polarization at the interface P_{J} is described as $P_{\mathrm{J}} = \left|G_{i,\uparrow} - G_{i,\downarrow}\right|/\left(G_{i,\uparrow} + G_{i,\downarrow}\right)$ by using

the interfacial conductions G_i, ρ_{N} and ρ_{F} are the resistivity of NM and FM, respectively.

Additionally, when the interface resistance is a tunneling barrier ($R_1,\ R_2 \gg R_{\mathrm{N}}$), Eq. (3.57) is modified as[112]

$$R_{\mathrm{s}} = P_{\mathrm{J}}^2 R_{\mathrm{N}} e^{-L/\lambda_{\mathrm{N}}} \tag{3.58}$$

Generally, since an insulating layer is inserted between NM and FM to avoid the conductivity mismatch, Eq. (3.58) is frequently used in the measurement of the nonlocal spin valves.

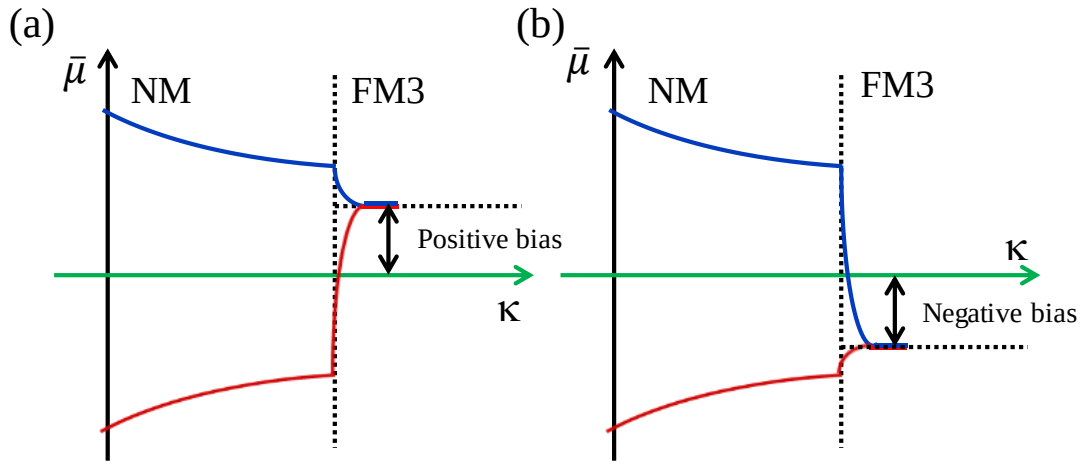

Figure 3.1: The schematic of the detected spin signal in the nonlocal spin valve measurements.

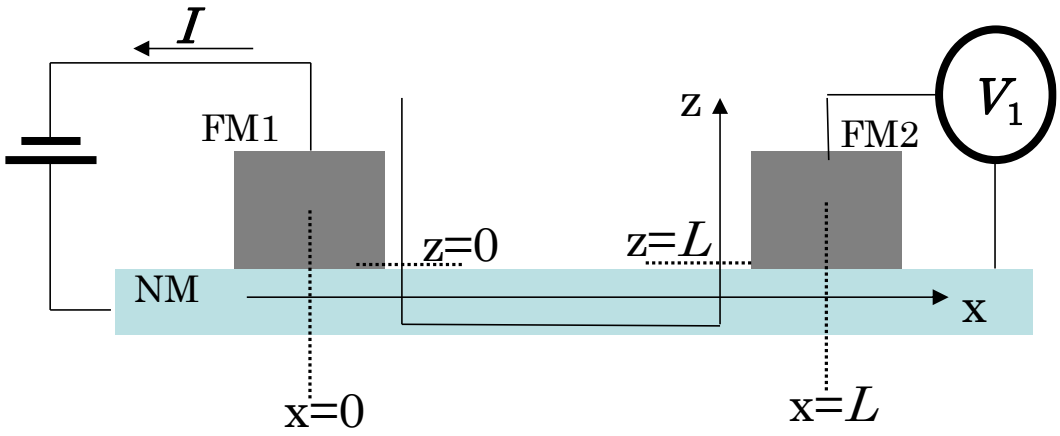

Figure 3.2: The schematic of the nonlocal spin valve devices. The z axis and the x axis is indicated.

Chapter 4

Electrical spin injection and spin transport in α-(BEDT-TTF)$_2$I$_3$ by the nonlocal spin valve measurements

4.1 Introduction

The understanding and manipulation of the spin transport in organic materials (OMs) have attracted considerable interest for fundamental material science and applications in the field of spintronics since the small spin-orbit interaction (SOI) in OMs consisting of light atoms leads to long spin relaxation times. In the past twenty years, a large number of spintronic devices based on OMs have been demonstrated (see Refs. [13, 69, 80, 113] and references therein), following the initial reports by Dediu et al. in 2002[21] and Xiong et al. in 2004[22]. The mechanism of spin transport in OMs is still one of the most important subjects to be clarified for their application to spintronic as above devices. Most devices reported so far have essentially been two-terminal devices in which the anisotropic magnetoresistance (MR) of the ferromagnetic metal (FM) electrodes and other spurious effects cannot be separated from the intrinsic spin transport effects in OMs.[13, 69, 85]

A nonlocal spin valve (NLSV), in which the charge current path is separated from the spin current path, is one of the most useful methods of studying spin transport.[89, 114, 115] Although there have been some reports on NLSV measurements of OMs, no clear signals from spin transport were detected.[99, 100, 101] Some groups prepared NLSV devices based on high-conductivity polymers such as PEDOT:PSS [99, 100] and pBTTT,[101] and discussed the reasons for the absence of spin transport signals. There are two possible

factors suppressing spin transport in NLSVs: one is the so-called conductivity mismatch[112] at the interface between conductive polymers and FM electrodes,[100, 101] and the other is the bipolarons in conductive polymers.[99] The conductivity mismatch[112] at the nonmagnetic/magnetic interface enhances the spin scattering since the typical electrical resistivity of conductive polymers (even heavily doped ones) is at least a few orders of magnitude higher than that of FM metal electrodes. It has been reported that inserting tunneling barrier layers between samples suppresses the effects of conductivity mismatch.[117, 92] Regarding the latter reason, it is reasonable in the absence of the spin-valve effect in doped conductive polymers, in which the bipolarons, which are spinless carriers, become dominant through the combination of polarons with increasing carrier concentration.[99, 118]

To overcome these difficulties, I prepared NLSV devices using a single crystal of the organic zero-gap conductor α-(BEDT-TTF)$_2$I$_3$ (abbreviated to α-I$_3$, where BEDT-TTF is bis(ethylenedithio)tetrathiafulvalene) as shown schematically in **Figure 1(a)**. α-I$_3$ is a quasi-two-dimensional conductor consisting of a conductive BEDT-TTF layer and an insulating I$_3$ layer.[119, 120] This I$_3$ layer may act as a tunneling barrier at the interface between the α-I$_3$ and FM $Ni_{80}Fe_{20}$ (Py) electrodes to avoid the conductivity mismatch as will be discussed later. At ambient pressure, α-I$_3$ shows metallic behavior with an electrical resistivity of approximately 0.01 Ωcm. At 135 K, it undergoes a phase transition to a charge-ordered insulator.[120] Under a high hydrostatic pressure of ≥ 1.5 GPa, this insulating phase is suppressed and a zero-gap conducting state appears. It has been reported that the carrier density n and carrier mobility μ decrease and increase with decreasing temperature, and reach 8×10^{14} cm^{-3} and 3×10^{5} cm^2/Vs at 2 K,

respectively.[121]

4.2 Experimental

In this study, I prepared an NLSV based on α-I_3 using a flexible polyethylene naphthalate (PEN) (Teijin DuPont Films Japan, Ltd.) substrate (**Figure 1(a)**) to avoid the damage to the α-I_3 crystal caused by the difference in the restriction coefficient between α-I_3 and an ordinary substrate under pressure.[122] The use of the PEN substrate enabled us to measure the nonlocal MR of an α-I_3 single crystal in a zero-gap conducting state. Eight FM electrodes were patterned on a PEN substrate by electron-beam lithography, which was followed by the electron-beam evaporation of a 30-nm-thick Py film (**Figure 1(b)**). A gold cap layer with a thickness of 10 nm was deposited on the Py film, which protected the electrodes from I-induced corrosion. **Figure 2** shows the microphotograph of the patterning of ferromagnetic electrodes. Without the gold layer, the Py film became corroded and the α-I_3 was also degraded as shown in **Figures 3**. Figure 3(a) shows the microphotograph of the Py thin films with an α-I_3 single crystal, which was taken immediately after attaching α-I_3. Figure 3(b) shows the microphotograph of the same sample taken an hour later. The Py film was obviously corroded by α-I_3 single crystal. Four electrodes were selected for nonlocal measurement so that the channel length (L) in the same crystal could be altered in the range from 700 to 1500 nm. The widths of the inner adjacent electrodes differed from each other (400 and 600 nm), resulting in the generation of different coercive forces.

Thin single crystals of α-I_3 were electrochemically synthesized. A current of 1 μA was applied to a chlorobenzene solution (20 ml) consisting of BEDT-TTF (10 mg)

and $[CH_3(CH_2)_3]_4N \cdot I_3$ (50 mg) for 6 h to yield platelike single crystals. The dimension of typical single crystals used in this experiment was approximately 200 μm × 25 μm × 150 nm. The thickness was measured by the step profiler. The crystals were dispersed in chlorobenzene and added dropwise to a PEN substrate. After the evaporation of the chlorobenzene, the crystals were strongly attached to the substrate by van der Waals forces (**Figure 1(b)**). Each sample was placed in a Teflon capsule filled with a pressure medium (Daphne 7373 oil), and the capsule was subjected to a pressure of up to 1.6 GPa in a clam-type pressure cell made of BeCu. The measurements were performed in a Quantum Design Physical Property Measurement System with a dc current source (Yokogawa GS210) and a nanovoltmeter (Agilent 34420A). The magnetic field was swept between −500 and 500 Oe at a rate of 2 Oe/s.

4.3 Results and Discussion

Before the nonlocal spin valve measurements, I confirmed the coercive field of Py electrodes. Figure 4 shows the magnetization (M) curve of Py electrode with a width of 400 nm, 600 nm and Py thin films as a function of magnetic field (B), measured by a SQUID magnetometer (Quantum Design). One can see the difference of coercive field of each Py. In addition, I also measured magnetization curve of Py electrodes, which is in device configuration as shown in Figure 2. Figure 5(a) indicates the magnetization curve, and Figure 5(b) shows dM/dB as a function of B. In Figure 5(b), one can see the six peaks indicated by arrows. The peaks indicated by black arrows represent coercive field of the Py pads which connect Py electrodes and Au lead wire. The peaks indicated by red and blue arrows represent coercive field of the Py electrodes with a width of 600 nm and 400 nm, respectively.

Next, I estimate the contact resistance R_i at the interface between Py/Au electrode and α-I_3 single crystals by using quasi 4 probe measurements. Figure 6(a) shows the results of 4 prove measurements and quasi 4 probe measurements, which indicated the contact resistance was approximately 500 Ω. This value is comparable to the resistance of α-I_3 single crystals (< 200 Ω). Figure 6(b) shows dV/dI as a function of I, which also revealed the contact resistance worked as a tunneling barrier between Py/Au electrodes and α-I_3 single crystals.

I show the temperature dependence of the resistance change ($R_T/R_{300\ K}$) of an α-I_3 single crystals itself (black curve), and that on PEN (red curve) and on PET (polyethylene terephthalate) (blue curve) under 1.6 GPa in Figure 6. For the α-I_3 single crystal on PET substrate, the resistance of α-I_3 increased with decreasing temperature. The temperature dependence of α-I_3 on PEN substrate is very similar to that of α-I_3 single crystal itself. This means that the influence of the PEN substrate on α-I_3 is lower than that of the PET substrate.

I measured the temperature T dependence of the resistance and the Hall mobility μ of the specimen to ensure that the hydrostatic pressure was properly applied to the samples. Figure 7 shows the Hall coefficient from 30 K to 4 K. One can see the steep drop of the Hall coefficient around 21 K, which reveals that the charge carriers in α-I_3 single crystals is changed from electrons to hales. The four-terminal resistance was almost independent of T from 300 to 2.5 K, whereas n and μ decreased and increased, respectively, by four orders of magnitude (**Figure 8**). This behavior is qualitatively identical to the zero-gap conducting state of bulk crystals. n is slightly larger than that of bulk α-I_3 single crystal[121] at low T; this is probably because of the strain and/or doping

effect at the interface between α-I_3 and the plastic substrate, as demonstrated by Tajima et al.[123] According to the energy dispersion, the carrier density satisfies the following formula:

$$n = \frac{\pi^2}{6C} \frac{k_B^2}{\hbar^2 v_F^2} T^2, \tag{4.1}$$

where C (= 1.75 nm) is the lattice constant along the direction normal to the two-dimensional plane, v_F is the effective Fermi velocity, $\hbar$ is the reduced Planck constant, and k_B is the Boltzmann constant.[121] I estimated v_F to be 2.5 × 10^4 m/s from the T dependence of the Hall coefficient. Furthermore, according to Mott's argument, the mean free path l of the carriers cannot be shorter than the carrier wavelength. In the case that scattering centers with high density exist, $k_F l \sim 1$ (where k_F is the Fermi wave number) and the sheet resistance approaches $0.5h/e^2$ (where e is the elementary charge). According to the report by Tajima et al. on the resistivity of α- I_3 single crystals,[121] the sheet resistance is comparable with the resistivity per layer (12.9–77.4 kΩ at 2 K) since α-I_3 is a layered material consisting of conductive and insulating layers as shown in Fig. 1. They have also mentioned that $k_F l \sim 1$ is valid for α-I_3 under pressure when the sheet resistance coincides with h/e^2 within a factor of five. The sheet resistance of our sample was 57 kΩ (~ $2 \times h/e^2$) at 2.5 K, which was nearly equal to that of bulk crystal.[121] It was thus considered that the condition $k_F l \sim 1$ was satisfied in our sample. Substituting the effective k_F estimated from $nC = 2\pi k_F^2 / 4\pi^2$, the mean free path was calculated to be l = 30 nm. As a result, D $(= 0.5 v_F l)$ was estimated to be 3.75 × 10^{-4} m^2/s for this sample.

To observe nonlocal MR in high-resistivity materials, a thin insulating layer

between the FM electrodes and the nonmagnetic channel is necessary to avoid a conductivity mismatch. When the interface resistance is sufficiently large for tunneling carrier injection to occur, the change in the nonlocal resistance ΔR can be described as follows:[112]

$$\Delta R = \frac{P^2 \lambda_s}{\sigma A} exp(-L/\lambda_s), \tag{4.2}$$

where P and σ denote the effective spin polarization of the FM electrodes and the conductivity of the nonmagnetic material, respectively. A is the device area calculated by multiplying channel width (~ 25 μm) by channel thickness (~ 150 nm). The above formula is valid for $R_i \geq \lambda_s / \sigma A$, where R_i is the contact resistance.[112] I measured R_i using four-terminal and quasi-four-terminal configurations, and found that when the above condition is satisfied, the spin diffusion length should be $\lambda_s \leq 7.7$ μm. As shown below, this condition was clearly satisfied by the sample examined in this study.

At 2.5 K, hysteretic MR with a ratio of 0.06% was observed in the two-terminal local measurement for L = 1300 nm, as shown in the upper panel of **Figure 9(a)**. In general, the voltage change associated with spin signal in two terminal (2T) measurement is twice of that in non-local configuration and shows opposite sign, as was discussed by Jedema et al.[124] The local MR observed in our device did not show this relation. This is most likely because the magnitude of local 2T signal consisting of spin accumulation was much lower than that of spurious MR such as anisotropic MR of ferromagnetic electrodes itself. The magnetic domain walls in the FM electrodes change the resistance of the FM electrodes during the magnetization reversal of the FM electrodes. Since it is difficult to clarify the origin of MR in local measurement, nonlocal measurement is necessary. In nonlocal MR measurements, the charge current path is separated from the spin current

path; the former flows anisotropically, while the latter flows isotropically. As shown in the lower panel of **Figure 9(a)**, the voltage switching of approximately 14 mΩ was observed in the nonlocal configuration. The observed loop looks like that of spin-valves, as was generally observed for the non-local measurement.[89, 114, 115] The variation in the nonlocal voltage at the switching field was almost proportional to the bias current up to ±500 μA (**Figure 9(b)**). The baseline resistance was approximately 8.2% of the four-terminal resistance (**Figure 9(c)**). No baseline MR was observed in the non-local measurement while the local four-terminal resistance exhibited a bulk MR of approximately 1.4 %. These findings imply that the charge current path was well separated from the electrodes during voltage detection in the nonlocal configuration, supporting the hypothesis that the spin-valve like MR loops originate from intrinsic spin transport.

The nonlocal MR decreased with increasing L as shown in **Figure 9(d)**. The exponential slope gives λ_s = 1.1 μm from Eq. (1). Furthermore, the value of D along with the relation $\lambda_s = \sqrt{D\tau_s}$ yields τ_s = 3 ns. It is interesting to compare these values with those of graphene since graphene is a representative zero-gap conductor and a promising spin transport medium owing to its small SOI and long spin relaxation time and spin diffusion length.[125] In comparison with those of graphene devices, α-I_3 has a long or comparable τ_s value, whereas λ_s is shorter[95, 126] owing to the lower D value than that of graphene NLSV devices (for which D is approximately 0.05 m^2/s [95, 126]).

There are two major differences between α-I_3 and graphene. First, the slope of the Dirac cone of α-I_3 is moderate and anisotropic.[120,123] The moderate slope reduces the Fermi velocity and D, although the effect of the tilted cone on the spin transport is unclear.

Second, the SOI in α-I_3 is considered to be larger than that in graphene because α-I_3 contains heavier atoms, such as sulfur and iodine. Although these properties of α-I_3 most likely reduce the spin diffusion length λ_s and the spin relaxation time τ_s, it is interesting that I could obtain comparative or higher values than those for graphene devices. This is probably because the spin scattering induced by surface defects/contamination and the effect of the substrate[115] is considered to be less than that in graphene devices owing to the multilayered structure of α-I_3. In addition, the inversion asymmetry, which generates an extra term in the equation for the SOI, also might be reduced in layered structures, as has been reported for graphene encapsulated in boron nitride with a multigate configuration.[115] Multilayer graphene has a longer spin diffusion length and spin relaxation time than single-layer graphene.[127] These aspects are important for designing OMs as a spin transport medium.

It has been reported that graphene changes its spin transport behaviors depending upon the substrates, which makes it difficult to clarify the spin relaxation mechanisms.[128] It is useful to consider the spin relaxation ratio $\varepsilon = \tau_p/\tau_s$ for discussing a spin transport property.[91] Here, τ_p is momentum relaxation time. **Table 1** summarizes the experimental date of carrier and spin transport properties for α-I_3 together with those for graphene on various substrates. The spin relaxation ratio of graphene on SiC and multilayer graphene are an order of magnitude smaller than those of graphene on SiO_2 and h-BN. Graphene on SiC is epitaxially grown on carbon-rich surface, which is electrically inactive and only weakly interacts with graphene layers,[97] resulting in long τ_s and low ε. Multilayer graphene can suppress spin scattering from the surface and the substrate.[126] I can see the spin relaxation ratio of α-I_3 (4×10^{-4}) is comparable to that of

graphene on SiO_2 and h-BN. The α-I_3 crystal contains heavy atoms such as iodine and sulfur, which enhances SOI. The spin scattering from the substrate is thought to be suppressed in layered structure of α-I_3 like graphene, resulting in low spin relaxation rate of α-I_3.

According to theoretical calculations,[129, 130] the spin relaxation times of the EY and DP mechanisms are $\tau_s^{\mathbf{EY}} \sim (\hbar v_{\mathbf{F}} k_{\mathbf{F}} / \Delta)^2$ and $\tau_s^{\mathbf{DP}} \sim (\hbar / \Delta)^2 / \tau_p$, respectively, where Δ is the spin-orbit coupling strength. Therefore, $\tau_s^{\mathbf{EY}} / \tau_s^{\mathbf{DP}} \sim (k_{\mathbf{F}} l)^2$; that is, the spin relaxation times of the EY and DP mechanisms are comparable to each other if $k_{\mathbf{F}} l \sim 1$. When I assume that $\tau_s^{\mathbf{EY}} = \tau_s^{\mathbf{DP}} = 2\tau_s \sim$ 6 ns, a Δ value of approximately 0.09 K is derived from τ_s and τ_p (= $l/v_{\mathbf{F}}$). This value is larger than the intrinsic SOI (~0.01 K) and comparable to the Rashba SOI (~0.07 K at 50 V/300 nm) in graphene.[129] Thus, the effective SOI in α-I_3 appears to be similar to that in single layer graphene on SiO_2.

Note that the T dependence of ΔR (**Figure 10**) monotonically decreased by a factor of approximately three as T increased from 2.5 to 300 K. The change of ΔR was much moderate comparing to that of the mobility and carrier density of α-I_3, which show a steep decrease and an increase, respectively, with increasing temperature as shown in Fig. 2. This correlation between ΔR and the mobility and carrier density implies that a dominant spin relaxation mechanism of α-I_3 change to EY from DP mechanism with increasing temperature. To modulate the mobility in the same sample by several orders of magnitude would provide new information for spin transport mechanism in materials.

4.4 Conclusion

In summary, I have developed a fabrication process for spin valves of a molecular conductor on a flexible polymer substrate to which a high hydrostatic pressure can be applied. Following the implementation of this technique, I performed NLSV measurements on the resultant α-I_3 organic zero-gap conductor at 1.6 GPa. Hence, a distinct nonlocal MR that decays with increasing gap distance was observed in an OM for the first time. The spin diffusion length and spin relaxation time were estimated to be 1.1 μm and 3 ns, respectively. The SOI calculated from the spin relaxation time and carrier lifetime was 90 mK. The diffusion constant of α-I_3 was one or two orders of magnitude smaller than that of graphene, resulting in a shorter spin diffusion length than that of graphene. On the other hand, the layered structure of α-I_3 exhibited a long spin relaxation time and a small SOI since it reduced spin scattering from the surface and the inversion asymmetry, which generates an extra term in the equation for the SOI. These findings provide guiding principles for materials design in organic spintronics.

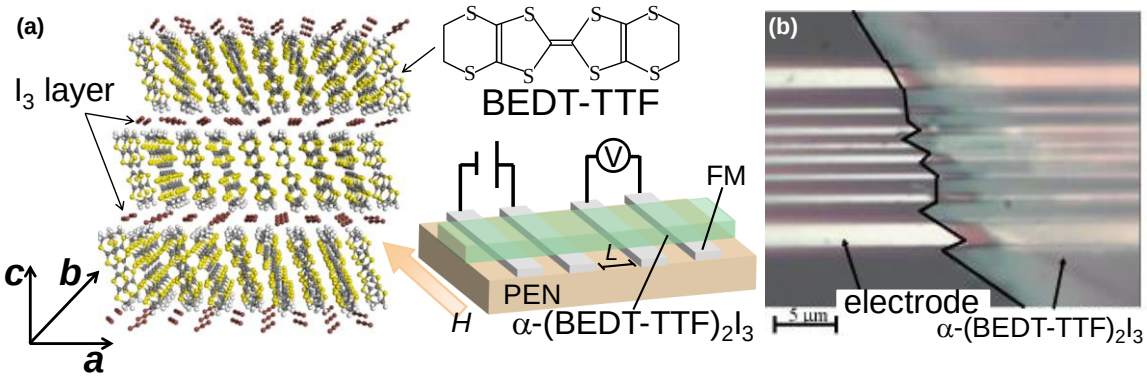

Figure 1. (a) Schematic of crystal structure of α-$(BEDT\text{-}TTF)_2I_3$ and nonlocal spin valve devices. The structural formula of a BEDT-TTF molecule is also shown. (b) Optical microscope image of lateral spin valve based on α-I_3 fabricated on a flexible PEN substrate. The solid line in the figure represents the edge of the crystal.

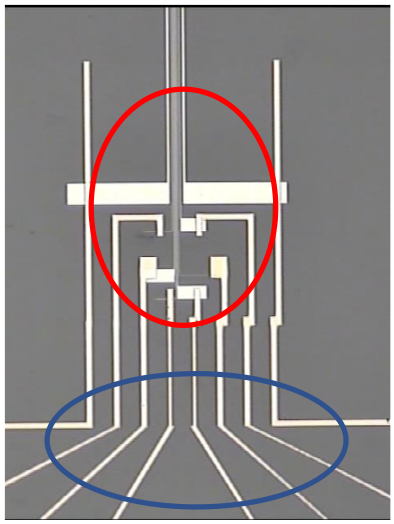

Figure 2. Optical microscope image of Py/Au electrodes and Au lead wires patterning. The thin lines surrounded by the blue open circle are Au lead wires, and the thin lines surrounded by red open circles are the Py/Au electrodes.

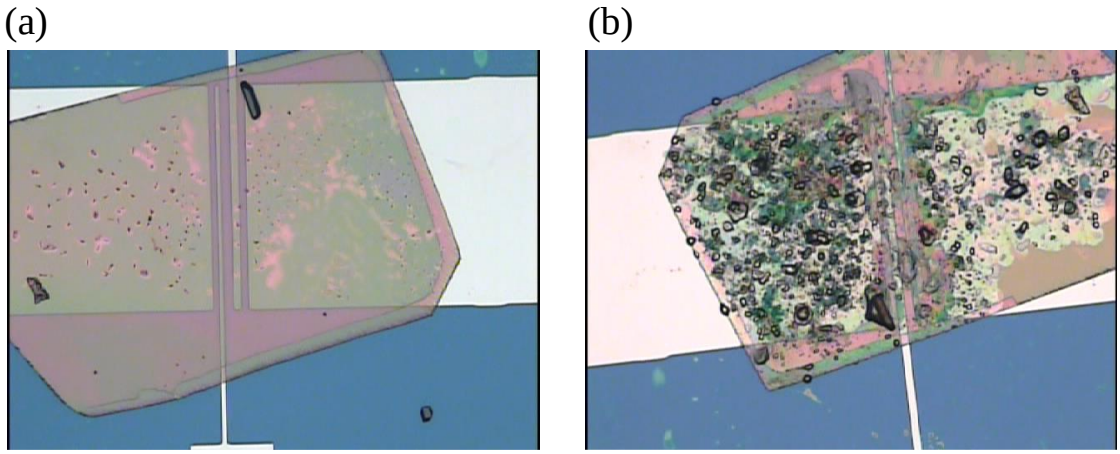

Figure 3. Optical microscope image of Py thin film contacting α-I_3 single crystal, which was taken immediately after putting α-I_3 single crystal (a), and which was taken an hour later form Figure 3(a) (b).

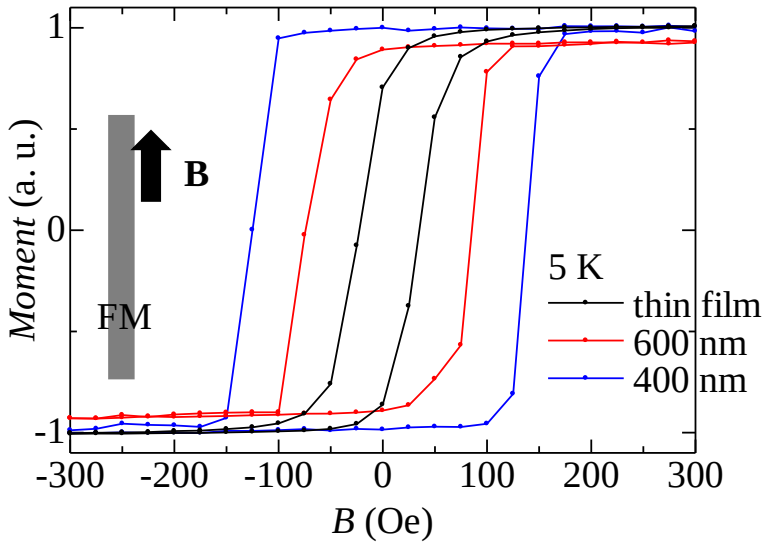

Figure 4. Magnetization of Py/Au electrodes as a function of magnetic field (M-H) measured by a SQUID magnetometer. Blue, red and black curves represent the M-H curves of Py with a width of 400 nm, 600 nm and Py thin film, respectively.

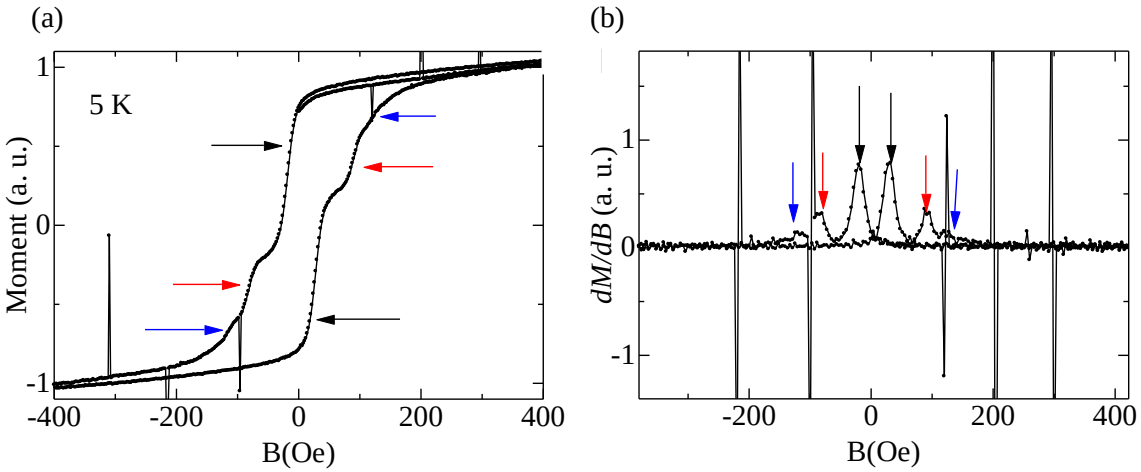

Figure 5. Magnetization curve of Py/Au electrodes, which is in device configuration as shown in Figure 2 as a function of magnetic field (a), and d*M*/d*B* curve (b).

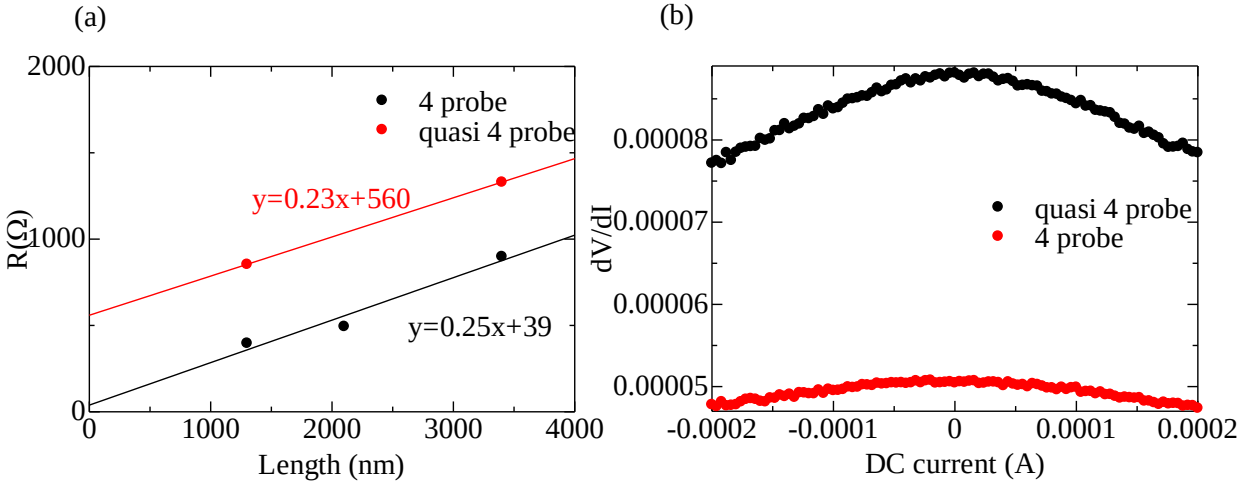

Figure 6. (a) The resistance of α-I_3 single crystal in device configuration measured by 4 probe (black) and quasi 4 probe (red) techniques, respectively. (b) the d*V*/d*I* characteristics as a function of *I*.

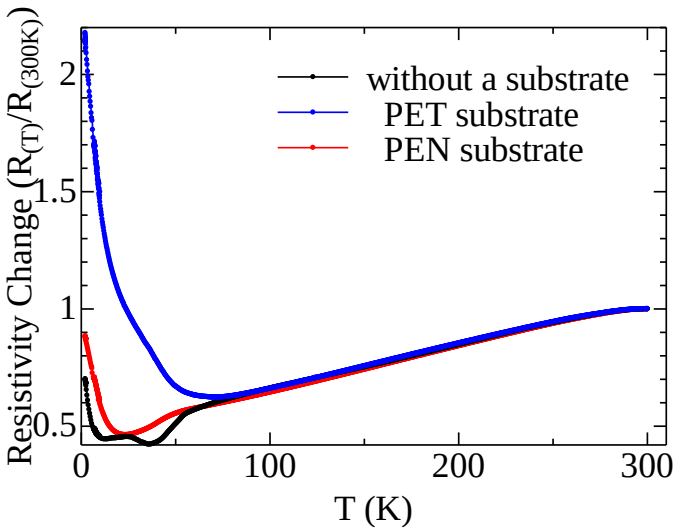

Figure 6. The temperature dependence of the resistance change of α-I_3 single crystals under 1.6 GPa on PEN substrate (red curve), PET (polyethylene terephthalate) substrate (blue curve) and without substrate (black curve)

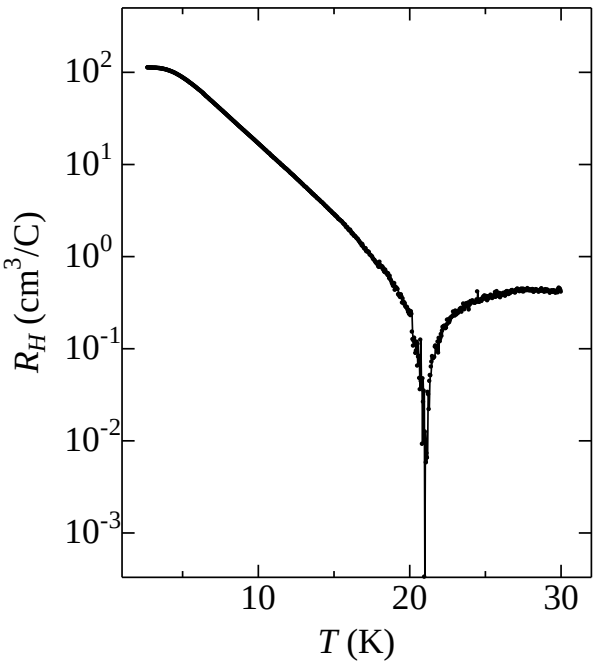

Figure 6. The Hall coefficient from 30 K to 4 K of α-I_3 single crystals.

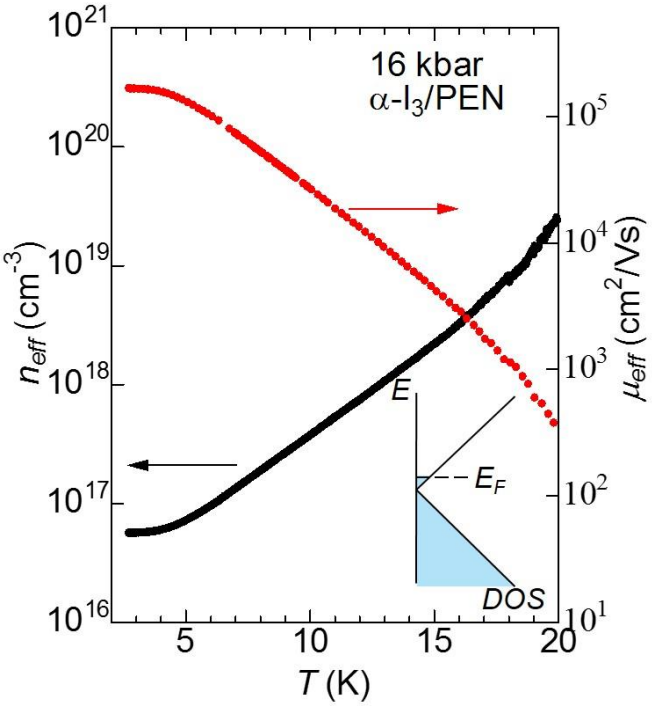

Figure 8. Hall effect of α-I_3 single crystal on a flexible polyethylene naphthalate (PEN) substrate. Dependence of effective carrier density (n_{eff}) and mobility (μ_{eff}) on temperature (T) derived from Hall effect in thin α-I_3 single crystal on PEN under a pressure of 1.6 GPa.

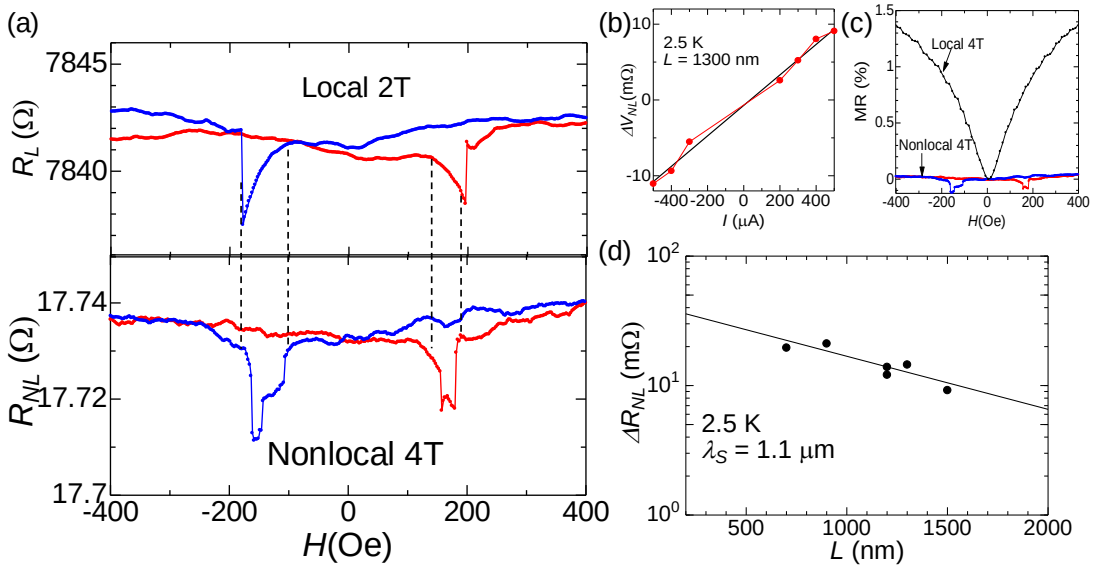

Figure 3. Spin valve characteristics of local and nonlocal MR. (a) Dependence of local two-terminal (2T) and nonlocal four-terminal (4T) resistance on magnetic field at 2.5 K. (b) Dependence of voltage drop on bias current at switching field in nonlocal 4T configuration. (c) MR ratios in local 4T and nonlocal 4T measurements. (d) Dependence of change in nonlocal resistance ΔR on gap length.

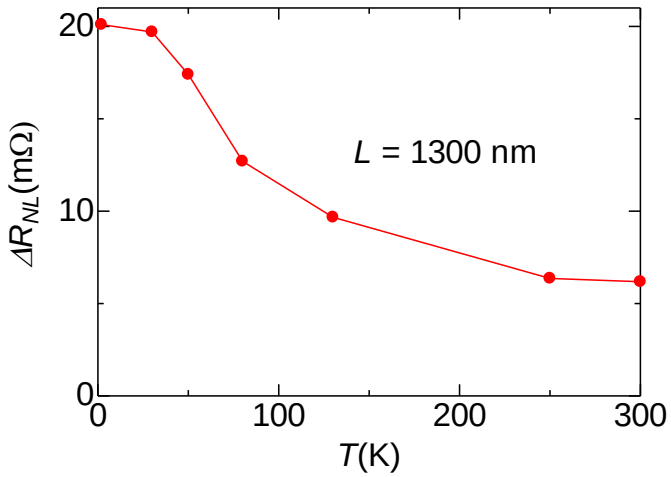

Figure 4. Dependence of nonlocal 4T MR on temperature (T) for 1300 nm gap spacing. ΔR monotonically decreases with increasing T.

Table 1. Carrier transport and spin transport properties of graphene on SiO2, SiC, h-BN, suspended graphene and multilayer graphene.

Material	μ ($cm^2V^{-1}s^{-1}$)	D_c (m^2s^{-1})	t_s (ps)	λ_{sf} (□m)	t_p (fs)*	ε **
Graphene on SiO_2 [95]	2×10^3	2×10^{-2}	100	1.5 – 2	40	4×10^{-4}
Graphene on SiC [97, 131]	2×10^3	2×10^{-2}	2300	0.5 – 1	40	1.7×10^{-5}
Graphene on h-BN [98]	4×10^4	5×10^{-2}	200	4.5	100	5×10^{-4}
Multilayer graphene [127]	—	1×10^{-2}	500 – 600	2.5 – 3	20	4×10^{-5} – 3.3×10^{-5}
α-I_3 [this study]	1×10^5	3.7×10^{-4}	3000	1.1	1200	4×10^{-4}

* τ_p is momentum relaxation time estimated by $D = 0.5 v_F l$

** ε is spin relaxation ratio ($= \tau_p / \tau_s$)

Chapter 5

Tunneling anisotropic magnetoresistance in $La_{0.7}Sr_{0.3}MnO_3$/pentacene/Cu/Au structure prepared on $SrTiO_3$ (110) substrate

5.1 Introduction

Since the pioneering works by Dediu et al.[21] and Xiong et al.,[22] spin injection and transport phenomena in organic materials (OMs) have attracted considerable interests because their low spin-orbit interaction leads to a long spin relaxation time for charge carriers in OMs.[132] The understanding and controlling of the interface between OMs and ferromagnetic metal (FM) electrodes have been important topics to be clarified for the application of OMs to spintronic devices. There have been several reports on interface effects such as spin-dependent hybridization,[33, 104, 133] interfacial spin selectivity[134–136] and magnetic anisotropy[70, 103, 137] in device structures, which could open new possibilities for spintronic devices.

Tunneling anisotropic magnetoresistance (TAMR) is also an interface effect between an FM electrode with magnetocrystalline anisotropy and mediums[138] including inorganic semiconductors (GaAs[139, 140]), metal oxides (MgO/CoFe,[141] MgO/Ta[142]) and OMs (PTCDI-C4F7[68], Alq_3[69]), in which the tunneling resistance depends on the magnetization direction of the FM electrode. The signal of TAMR is much larger than that of the anisotropic magnetoresistance (AMR) observed in the FM electrode itself.[68] There have been reports on the TAMR of OMs on Co[113, 143] and $La_{0.7}Sr_{0.3}MnO_3$ (LSMO) [68, 69, 144] electrodes. Barraud et al. demonstrated that electronic hybridization between Co

and Co-phthalocyanine induced uniaxial magnetic anisotropy at the interface, which dramatically changed the TAMR effect.[113] In addition, by calculation of the TAMR effect in a magnetic tunnel junction of LSMO and $SrTiO_3$ (STO), Burton and Tsymbal showed that the out-of-plane magnetization of LSMO had ~500% higher junction resistance than the in-plane magnetization.[145] These reports show the possibility of enhancing the TAMR ratio by active control of the interface between OMs and FMs.

I prepared TAMR devices consisting of epitaxial LSMO thin films on STO (110) substrates and thermally evaporated pentacene (100 nm in thickness)/Cu (5 nm)/Au (17 nm) layers, as shown in Fig. 1. I measured the dependence of the TAMR on the magnetic field (***B***) strength and the ***B*** angle. Although these two measurements generally showed almost the same TAMR ratio, it was found in the present experiment that the TAMR ratio in the ***B*** strength dependence (14%) was approximately ten times larger than that in the ***B*** angle dependence (1.5%) at a high magnetic field, which is probably owing to the out-of-plane component of the magnetic anisotropy of LSMO thin films generated by the tensile strain applied to them.[146, 147] This result suggests that the control of the out-of-plane component of the interface magnetic anisotropy enhances the magnetoresistance (MR) ratio.

5.2 Experimental

Figure 1 shows a schematic of the device. It was a so-called cross-bar type device with a layered structure of LSMO (20 nm in thickness)/pentacene (100 nm)/Cu (5 nm)/Au (17 nm). An LSMO film (1.5 mm in width) was grown on STO (110) maintained at 1073 K by pulsed laser deposition according to the previous reports by Boschker et al[147] and by Huijben et al.[148] using a 248 nm KrF laser (200 mJ, 5 Hz) under an oxygen pressure

of 40 Pa. The LSMO film was annealed at 1073 K for 15 min under an oxygen pressure of 4 Pa. Epitaxial growth of LSMO on STO(110) was confirmed by using reflection high energy electron diffraction. The [001] and [$1\bar{1}0$] axes of LSMO were parallel to those of STO. The crystal structure of the grown films was investigated also by X-ray diffraction. Pentacene layers were thermally evaporated from a Knudsen cell with an evaporation rate of 3 nm/min under a pressure of 1×10^{-5} Pa. The pentacene (Aldrich 99.8 %) was used after purification. The thickness of the pentacene layers was 100 nm, as estimated with a step profiler. The top Cu electrode (1.0 mm in width) was deposited by e-beam evaporation. A Au capping layer was then thermally evaporated to complete the device. The active area was estimated to be approximately 1.5 mm^2. All measurements were carried out in a liquid He cryostat (Physical Property Measurement System (PPMS), Quantum Design) under a pressure of 500 Pa at 4 K. A magnetic field $\boldsymbol{B}$ in the range from -3000 Oe to 3000 Oe was applied along the in-plane angle θ (see Fig. 1). The angles θ = 0° and 90° correspond to the [001] and [$1\bar{1}0$] axes of LSMO, respectively. A bias voltage was applied to the bottom LSMO with respect to the electrically grounded top Au electrode. Magnetization was measured with a SQUID magnetometer (Quantum Design) as a function of magnetic field (M-H).

5.3 Results and discussion

Figure 2(a) shows a plot of the X-ray θ-2θ diffraction spectrum of LSMO on STO (110). Peaks assigned to (h k 0) for STO and LSMO can be seen. The interplanar distance of the LSMO (110) planes was estimated to be approximately 0.273 nm, which is consistent with a previous report on LSMO thin films grown epitaxially on STO

(110).[147] The value is smaller than that for bulk crystal.[149] The shortened interplanar distance can be explained by tensile strain in the [001] axis induced by the STO (110). [147] Magnetization loops of LSMO films with ***B*** along the [001] and [1$\bar{1}$0] axes of the LSMO are shown in Figs. 2(b) and 2(c), respectively. When ***B*** was parallel to [001], the M-H curve was almost square, whereas it had a distorted rectangular shape when ***B*** was parallel to [1$\bar{1}$0]. This result agrees with a previous study indicating that [001] and [1$\bar{1}$0] axes of LSMO are easy and hard axes, respectively. [147]

The current-voltage (I-V) characteristics of the TAMR devices is shown in Figure 3. Typical TAMR devices showed the resistance of a few kΩ and the slightly nonlinear I-V characteristics and LSMO electrode showed the resistance of a few tens W with linear I-V characteristics as shown in Fig.3. Some devices with a thicker pentacene layer (ca. 300 nm estimated with a step profiler) showed the resistance of a few MΩ. The resistance of the TMAR device was not proportional to the thickness of the pentacene layer, as was frequently observed for layered organic devices, possibly because of the penetration of metal particles into organic films during the deposition of the top electrode. This ill-defined layer extends into the organic films up to the thickness of about 50–100 nm,[61] resulting in short-circuit or formation of tunneling paths in some devices. Actually, some of the devices prepared in the present experiment showed the resistance of a few tens Ω with a linear I-V characteristic, indicating short-circuit between the top and bottom electrodes. The temperature dependence of the resistance was moderate and it showed lower resistance at low temperature than that of room temperature (R_{5K}/R_{300K} ~ 0.4 at 0.1 V, R_{300K} was around 10 kΩ), while the resistance of the device with thick pentacene layer was increasing with decreasing temperature (R_{5K}/R_{300K} ~ 8 at 0.1 V, R_{300K} ~ several MW).

These characteristics is shown in Figure 4. In the previous studies on OSVs describes that the weak temperature dependence of the resistance of OSVs are attributed to tunneling transport through the organic layer, as pointed out to the organic spintronic devices using LSMO. [66, 67, 74] It is important to note that the device resistance in tunneling regime slightly increases or unchanged with decreasing temperature in those previous reports. However, in my experiments, the resistance of TAMR device decreased with increasing temperature as mentioned above. This characteristic is similar to the report by Sayani et al.[150] They reported that when the thickness of ill-defined layer was relatively thick, the device resistance decreased with decreasing temperature and I-V characteristics was slightly non-linear. According to the study by Sayani et al., the temperature dependence of the TAMR device resistance is dominated by the resistance of metal nanoparticles in ill-defined layer or by the tunneling resistance between nanoparticles.

It is well known that LSMO thin films show anisotropic magnetoresistance (AMR) depending on the magnetization direction. First, the AMR effect originating from the LSMO electrode is discussed. The resistance of LSMO electrodes and TAMR device was approximately 20 Ω and 7.7–7.8 kΩ, respectively. Figures 5(a) and 5(b) show the dependence of device resistance on the in-plane magnetic field angle θ without and with a pentacene/Cu/Au layer, respectively. The magnetic field $\boldsymbol{B}$ was 3 kOe, which is sufficiently high for saturation magnetization (see Fig. 2). Both graphs show an anisotropic resistance distribution with twofold symmetry. The MR ratio was calculated by $MR(\theta)(\%) = (R(\theta) - R(90°))/R(90°)$. One could see a typical MR ratio of 0.15% attributed to AMR in Fig. 3(a). On the other hand, the resistance anisotropy observed in Fig. 3(b) is 15 % at $\theta \sim 90°$. This large anisotropy shows the existence of TAMR[68] at the interface between LSMO (110) and pentacene, and indicates that the AMR effect is small

enough to be ignored, compared to the TAMR effect. Therefore, I do not take into account the effect of AMR in the following discussion. The LSMO without and with pentacene layer had different $MR(\theta)$ behaviors. The maximum value of $MR(\theta)$ of the LSMO electrode appeared around $\theta = 0°$ while that of the TAMR device appeared around $\theta =$ 30° as shown in Figs. 5(a) and 5(b), which implies a change of magnetic properties of LSMO electrodes induced by deposition of the pentacene layer.

Figure 6 shows the typical MR trace as a function of $\boldsymbol{B}$ at various angles in plane. The MR ratio was calculated using $MR(B)(\%) = (R(B) - R(3\text{kOe}))/R(3\text{kOe})$. The observed MR curves with a nonlinear background are similar to those in previous studies for TAMR,[68, 69] giant magnetoresistance (GMR) and tunneling magnetoresistance (TMR) in organic spin-valves.[22, 66, 74] The nonlinear background in organic spin-valves is known to originate from magnetic domains in FM electrodes. In our devices with a Cu top electrode, GMR and TMR should not occur. The AMR effect of the LSMO electrode itself can be ignored as mentioned above. It was thus concluded that the MR curves obtained for our devices were caused by TAMR. Figures 7(a) and 7(b) show the bias voltage dependence of TAMR and AMR signals, respectively. The TAMR signal decreased with increasing bias voltage as reported in the previous study,[143] while the AMR of the LSMO electrode hardly changed. This bias voltage dependence supports that the observed MR curves in Fig. 6 was originated from the TAMR effect.

Compared with previous studies of TAMRs in organic spin-valves, our device showed three different characteristics. First, the dependence of the TAMR ratio on the $\boldsymbol{B}$ strength (Fig. 6, $MR(B) \sim 14\%$) was approximately ten times larger than that on the $\boldsymbol{B}$ angle dependence (Fig. 5(b), $MR(\theta) \sim 1.5\%$). In the previous studies on TAMR, $MR(\theta)$ and $MR(B)$ showed almost the same since the TAMR depend mainly on in-

plane magnetization of FM electrodes.[68, 69, 113, 143, 144] Second, $MR(B)$ of our devices examined showed always positive sign. The TAMR devices reported so far change sign of $MR(B)$ from negative to positive depending on the in-plane $\boldsymbol{B}$ angle.[68, 69, 113, 143, 144] Third, the resistance switched around $\boldsymbol{B}$ ~ 1 kOe and 0.5 kOe when θ was close to the magnetization hard axis of LSMO [$1\bar{1}0$]. It is difficult to explain these behaviors by considering only the in-plane magnetization of LSMO. If a magnetization reversal of the LSMO electrode caused by external magnetic field $\boldsymbol{B}$ occurs only via the in-plane magnetization direction, the maximum value of $MR(\theta)$ and $MR(B)$ should be almost the same. Since a large resistance change was observed at low $\boldsymbol{B}$ in our measurements, I take the out-of-plane magnetization of LSMO at low $\boldsymbol{B}$ into account in the following discussion.

Boschker et al. have argued that LSMO thin films on STO (110) induce tensile strain along the [001] direction, resulting in a partially out-of-plane easy axis and the formation of magnetic domains in LSMO thin films.[147] The magnetization direction tends to align with easy axes rather than hard axes at low $\boldsymbol{B}$. Therefore, when the interfacial magnetic anisotropy has two or more easy axes, the dependence of the TAMR on $\boldsymbol{B}$ strength may show complicated behaviors such as double-step switching of the TAMR.[151] This is because the TAMR depends on the interfacial magnetization direction, which is affected not only by the $\boldsymbol{B}$ direction but also by the interfacial magnetic anisotropy. According to a theoretical calculation,[145] a large TAMR ratio resulting from the out-of-plane magnetization of LSMO is predicted since the tunneling transmission around the Fermi level changes dramatically between the in-plane and out-of-plane magnetization directions of LSMO.

It is considered that the inconsistency in the TAMR ratio between $MR(\theta)$ (~

1.5 %) and $MR(B)$ (~14 %) observed for our devices is also caused by the contribution of the out-of-plane magnetization of the LSMO at low $\boldsymbol{B}$. Strain-induced LSMO thin films on STO (110) have an easy axis with an out-of-plane component.[147] Since the value of the TAMR originating from the out-of-plane magnetization of LSMO is much larger than that originating from the in-plane magnetization, a sign change in $MR(B)$ from negative to positive depending on θ was not observed for our devices. Note that the TAMR behaviors at low $\boldsymbol{B}$ such as double-step switching[151] are induced by the complicated interfacial magnetic anisotropy of LSMO on STO (110), which has an easy axis with an out-of-plane component and many magnetic domains.[147]

Next, to support the discussion mentioned above, I indicate the TAMR effect in LSMO/Pentacene/Co structures prepared on STO (100) substrate. The thickness of the pentacene layer was approximately 300 nm measured by the step profiler. Comparing the result of the TAMR device prepared on STO (100) with on STO (110) should clarify the effect of strain-induced LSMO. First, Figure 8 shows a plot of the X-ray θ-2θ diffraction spectrum of LSMO on STO (100). Since the lattice mismatch between LSMO (100) and STO (100) is not appeared, peaks assigned to (h 0 0) for LSMO and STO cannot be separated, in which LSMO thin film is not influenced by strain-induced effect from STO (100) substrate.

Figure 9 shows the dependence of the device resistance on the in-plane magnetic field angle θ, as was measured in TAMR devices prepared on STO (110) substrate. One can see the strong TAMR effect, and $MR(\theta)$ for this TAMR device is approximately 9 %. Figure 10 shows the typical MR trace as a function of $\boldsymbol{B}$ at various angles in plane. When the angle of $\boldsymbol{B}$ is 120° and 180°, the sign of observed MR is positive and negative, respectively. The change of sign depending on the angle of in-plane $\boldsymbol{B}$ is typical

characteristics of TAMR effect as was reported in the previous report. [68, 69, 113, 143, 144] Figure 11 shows MR trace as a function of $\boldsymbol{B}$ at 120° and 180°. One can see that the difference of the resistance at high magnetic field between 120° and 180° is almost the same value of the TAMR effect at low magnetic field. $MR(\theta)$ (Figure 9, 9 %) and $MR(B)$ (Figure 11, 8 %) showed almost the same since the TAMR depend mainly on in-plane magnetization of FM electrodes. This characteristic is also consistent with the previous report on TAMR device. [68, 69, 113, 143, 144] However, this characteristic of TAMR behaviors prepared on STO (100) is completely different of that of TAMR device prepared on STO (110). This is because the existence of the strain-induced effect from STO(110) substrate changes the TAMR behaviors as mentioned above.

In this work, the device active area was designed to be approximately 1.5 mm^2 to obtain a sufficient current for measurements. This is much larger than the estimated magnetic domain size for LSMO on STO (110) (500 $\times$ 500 nm^2).[147] Because of this large active area, the MR curves have nonlinear backgrounds. The TAMR behaviors in the $\boldsymbol{B}$ strength dependence are considered to be affected by the magnetization of each magnetic domain.

5.4 Conclusion

This study demonstrated a large TAMR ratio due to the out-of-plane magnetization of strain-induced LSMO thin films on STO (110). It is expected that TAMR devices with higher performance can be achieved by active control of the interface magnetic anisotropy. In the present study, the axes giving the largest $MR(\theta)$ rotated by approximately 30° for the device with pentacene. It was reported that electrical hybridization between OMs and FMs induces out-of-plane magnetization[103] or changes

the interface magnetic anisotropy.[113] Furthermore, a molecular interface may make nonmagnetic metals ferromagnetic.[70] The interface engineering is expected to become increasingly important for future spintronics.

Figures

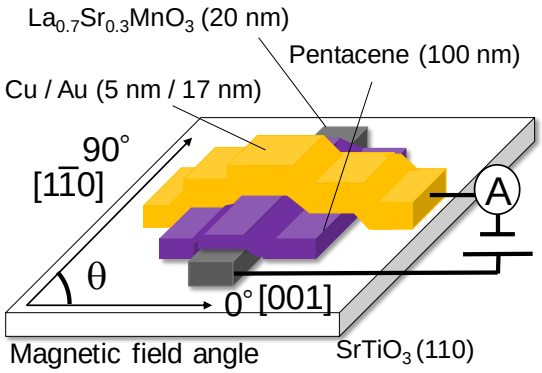

Fig. 1: Schematic of the organic TAMR device. From top to bottom: Cu/Au top electrode (5 nm/17 nm), pentacene layer (100 nm) and $La_{0.7}Sr_{0.3}MnO_3$ bottom ferromagnetic electrode (20 nm). The active area is 1.5 mm^2. An in-plane magnetic field is applied along the angle θ.

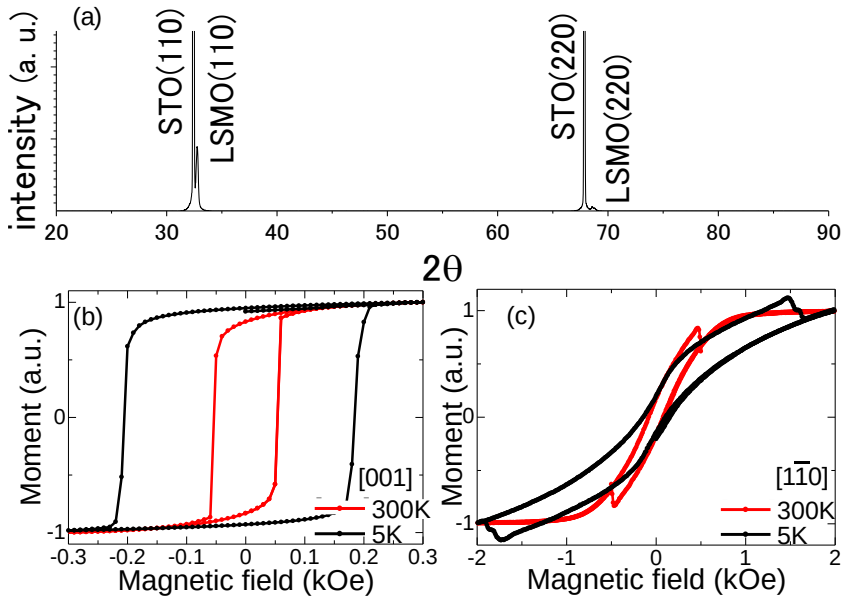

Fig. 2: (a) X-ray θ-2θ diffraction of the LSMO thin film on STO (110) substrate. (b) and (c) Magnetization as a function of magnetic field (M-H) along [001] (b) and [1$\bar{1}$0] (c), measured with a SQUID magnetometer. Red and black curves represent the M-H curves at 300 K and 5 K, respectively.

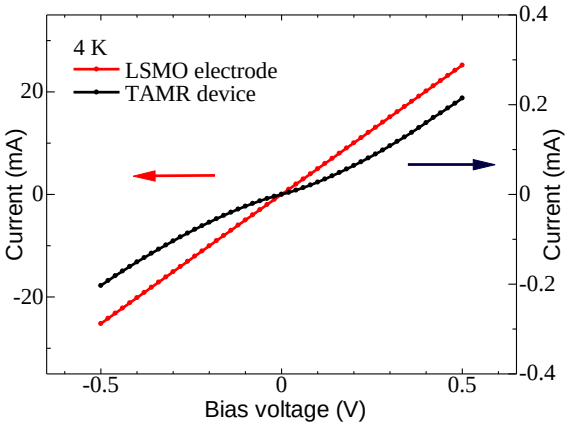

Figure 3: The current-voltage characteristics of a LSMO electrode (red curve) and a TAMR device (black line), measured at 4 K.

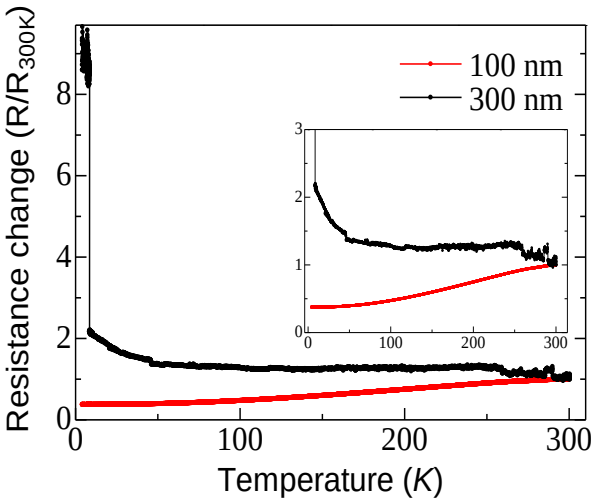

Figure 4: The temperature dependence of TAMR devices measured at 0.1V with 100 nm/300 nm thickness of pentacene (red/black curve).

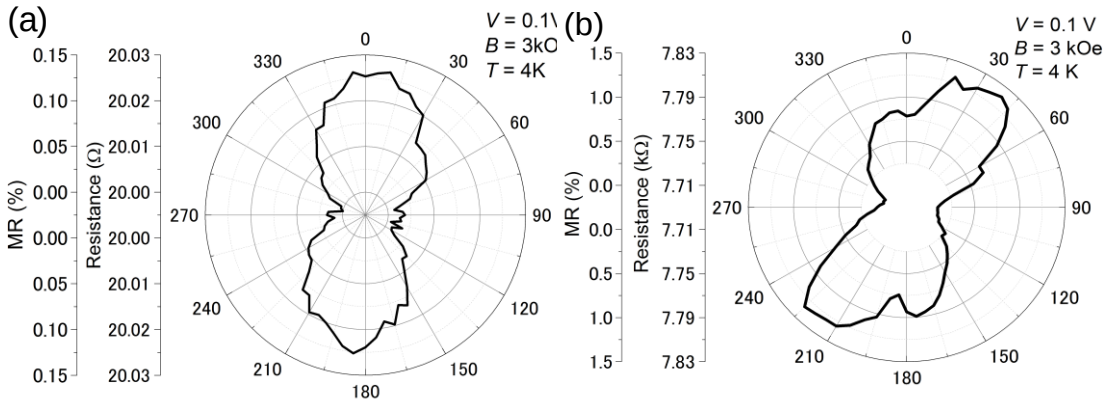

Fig. 5: Magnetoresistance scan taken at constant field (B = 3 kOe, bias V = 0.1 V) for devices without (a) and with (b) pentacene.

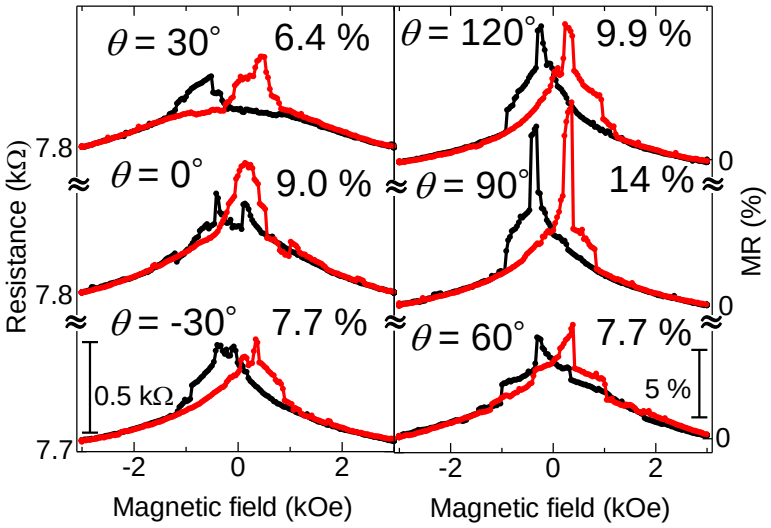

Fig. 6: Magnetoresistance at different angles θ of magnetic field, measured at 4 K with the bias voltage of 0.1 V. The red/black curves show that the magnetic field is swept from negative/positive to positive/negative. $\theta = 0^{o}$ is along the [001] direction of LSMO (110), and 90^{o} is along the $[1\bar{1}0]$ direction. The device resistance at 3 kOe was approximately 7.7–7.8 kΩ. Scale bars shown in the graph indicate a resistance of 0.5 kΩ and MR of 5 %.

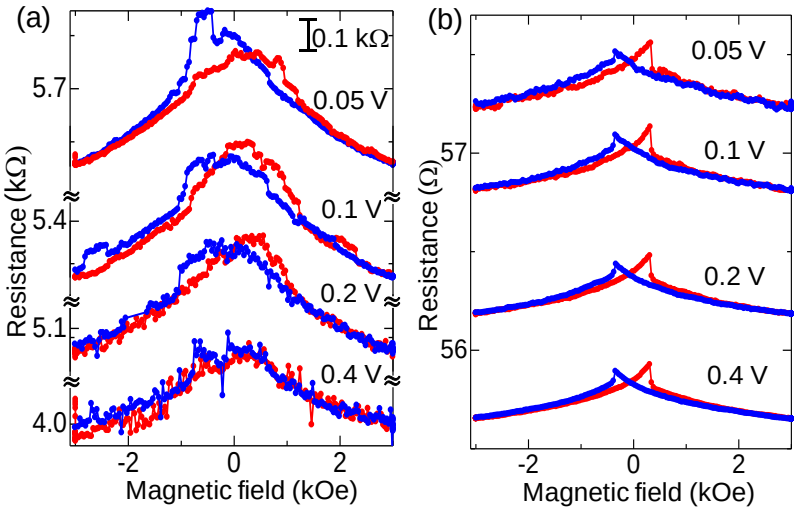

Fig. 7: The bias voltage dependence of TAMR (a) and AMR of the LSMO electrode (b). The magnetic field was applied along the [001] of LSMO. The scale bar in fig. 5(a) indicates the resistance of 0.1 kΩ.

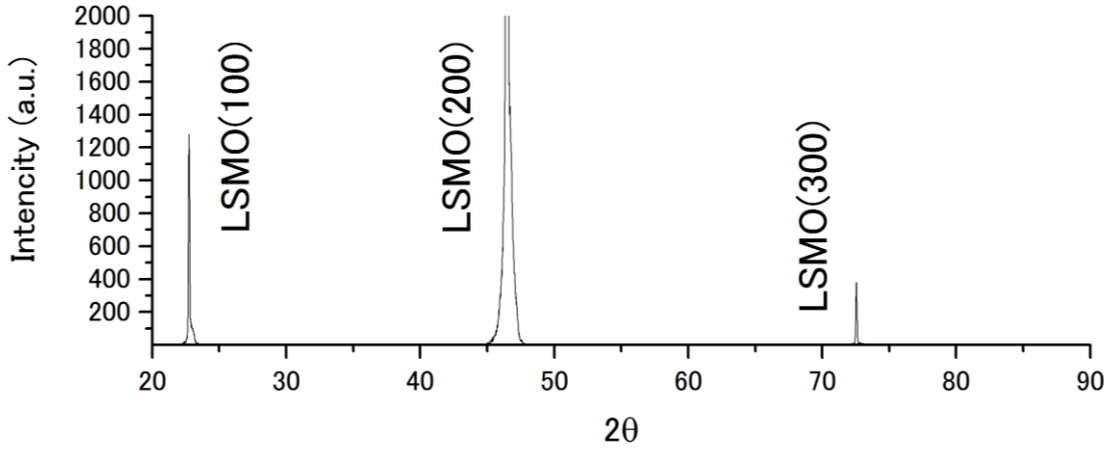

Figure 8: X-ray θ-2θ diffraction of the LSMO thin film on STO (100) substrate.

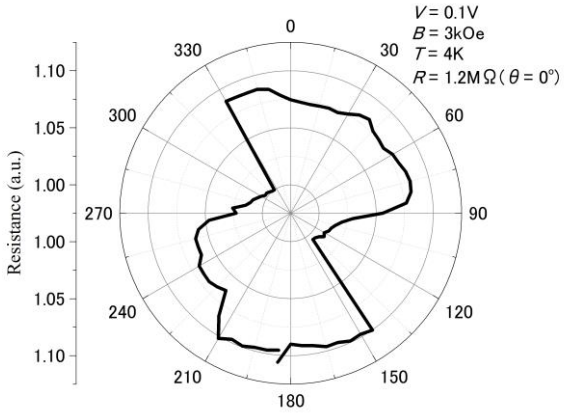

Fig. 9: Magnetoresistance scan taken at constant field (B = 3 kOe, bias V = 0.1 V) for devices prepared on STO (100) substrate.

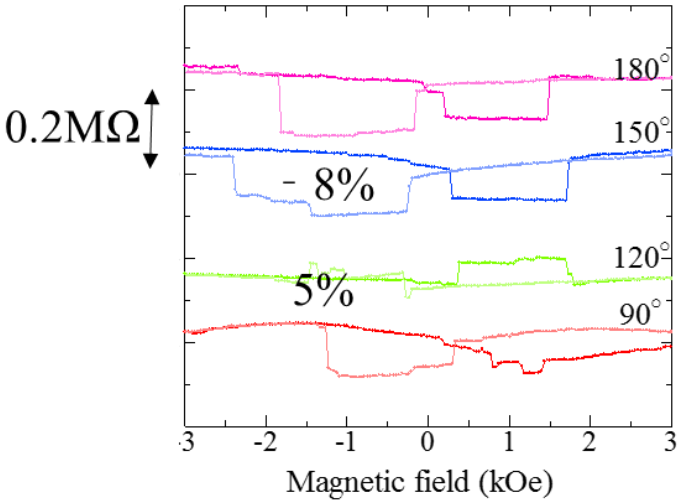

Fig. 10: Magnetoresistance of the TAMR device prepared on STO (100). TAMR is measured at different angles θ of magnetic field, measured at 4 K with the bias voltage of 0.1 V.

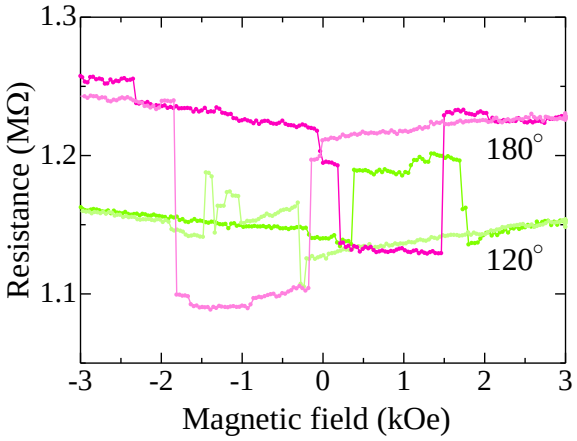

Fig. 11: Magnetoresistance at angles 120° (green curve) and 180° (red curve) of magnetic field, measured at 4 K with the bias voltage of 0.1 V.

Chapter 6

Conclusion

In this chapter, I summarize the results and discussions in this thesis and describes future plans.

6.1 Summary of chapter 4

I prepared nonlocal spin valves based on single crystals of an organic multilayered zero-gap conductor, α-I_3, and succeeded in evaluating the spin diffusion length (1.1 μm) and relaxation time (3 ns) at 2.5 K under a static pressure of 1.6 GPa for the first time, using a polyethylene naphthalate as a substrate. Although α-I_3 includes heavy atoms such as iodine, it exhibited a rather long spin relaxation time comparable to that of graphene. The SOI estimated on the basis of the experimental values of the spin relaxation time and carrier lifetime (1.2 ps) was 90 mK. The long spin relaxation time and small SOI evaluated for α-I_3 are considered to originate from its layered structure, in which spin scattering induced by surface defects is suppressed. In addition, the inversion asymmetry, which generates an extra term in the equation for the SOI, might be reduced in layered structures. These findings provide guiding principles for materials design in organic spintronics.

6.2 Summary of chapter 5

I investigated TAMR effects at the interface between pentacene and LSMO thin films prepared on STO (110) substrates. The dependence of the TAMR ratio on the magnetic field strength was approximately ten times larger than that of the magnetic field angle at

a high magnetic field. This large difference in the TAMR ratio is explained by the interface magnetic anisotropy of strain-induced LSMO thin films on a STO (110) substrate, which has an easy axis with an out-of-plane component. I also note that the TAMR owing to out-of-plane magnetization was positive at each angle of the in-plane magnetic field. This result implies that active control of the interface magnetic anisotropy between organic materials and ferromagnetic metals should realize nonvolatile and high-efficiency TAMR devices.

6.3 Future plans

6.3.1 Nonlocal spin valve measurements for other organic single crystals

It is important to investigate spin injection and spin transport in other OMs since α-I_3 single crystal under 1.6 GPa is a zero-gap conductor and has unique characteristics.

In this thesis, I chose α-I_3 for the sample of nonlocal spin valve measurements since I expected the high mobility of α-I_3 single crystals (more than 10,000 cm^2/Vs at low temperature) could realize large nonlocal MRs. However, as mentioned in chapter 4, I could observe the nonlocal MR at room temperature, in which the mobility of α-I_3 single crystals is relatively low (less than 10 cm^2/Vs at low temperature) This correlation between nonlocal MRs and the mobility implies that the nonlocal MRs is expected to be observed in low mobility organic conductors.

Here, I describe the results of nonlocal spin valve measurements for single crystal of organic conductor, β-$(BEDT\text{-}TTF)_2I_3$, of which crystal structure is different from that of α-I_3 single crystals. The mobility of β-$(BEDT\text{-}TTF)_2I_3$ is relatively low at low temperature. Figure 1 indicates the result of MR characteristics in the measurement

of nonlocal spin valves using β-(BEDT-TTF)$_2$I$_3$ single crystal at 2.5 K. However, it is difficult to regard this magnetoresistance as a spin signal originated from the pure spin current in β-(BEDT-TTF)$_2$I$_3$ single crystal. This is because when I measured the resistance of β-(BEDT-TTF)$_2$I$_3$ single crystal as a function of the magnetic field by local 4 probe measurement, the hysteresis curve depending on the magnetic field was observed as shown in Figure 2. In Figure 2, the black curve shows the result of local 4 probe measurement and red/blue curve shows the results of nonlocal magnetoresistance. From this results, I cannot specify the origin of the magnetoresistance in the local 4 probe measurement. One possible origin is the AMR effects from FM electrodes. This is because the AMR effect can be detected in local/nonlocal measurement when the spin current is not separated from the charge current, which form complicated current path in β-(BEDT-TTF)$_2$I$_3$ single crystal due to unclear interface between OMs and FM.

Although the nonlocal spin valve measurement of β-(BEDT-TTF)$_2$I$_3$ single crystal need further experiments, it is an attractive topic to measure nonlocal magnetoresistance of other organic conductors.

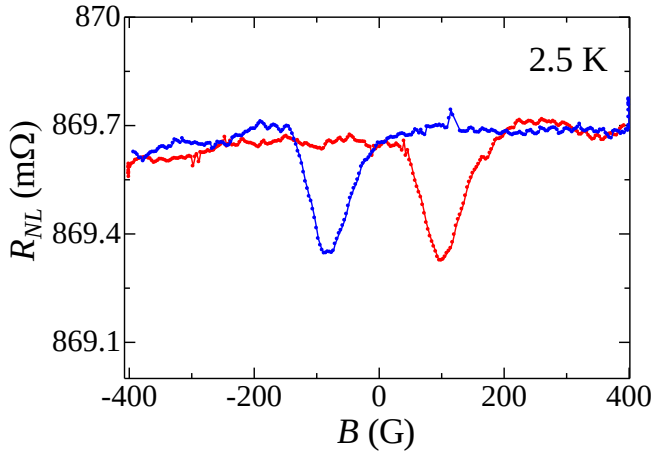

Figure 1. Magnetoresistance of β-(BEDT-TTF)$_2$I$_3$ in nonlocal spin valve measurements.

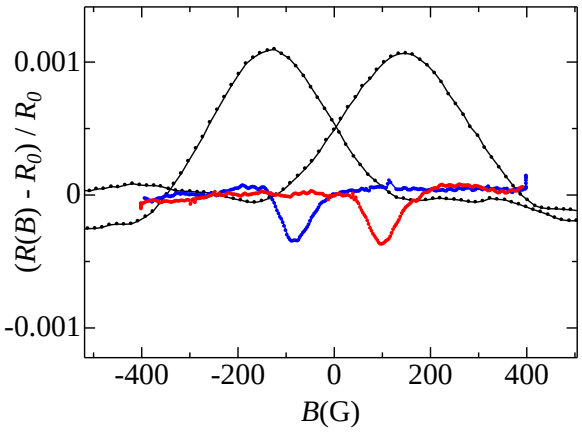

Figure 2. Magnetoresistance of β-(BEDT-TTF)$_2$I$_3$ in nonlocal spin valve measurements (black curve) and in local 4 probe measurements (red/blue curve) at 2.5 K.

6.3.2 Impact of molecules for TAMR effects

Since the structure of TAMR devices is more simple than that of OSVs using two FM electrodes, to investigate the TAMR effect between OMs and FM will promote the development of future spintronic devices based on interface MR.

In chapter 5, I described a change of magnetic properties of LSMO electrodes induced by deposition of the pentacene layer. However, the role of organic layer is still not clear. While I have changed the growth condition of the pentacene layer including substrate temperature and/or evaporation rate during deposition, we could not see noticeable change in TAMR behaviors. This is possibly because the electronic structure of the interface between first layer of pentacene and LSMO surface is not affected by such deposition condition. Therefore, the use of other organic materials such as C_{60} is a possible way to study TAMR behaviors depending on molecules. In addition to that, to

use Co thin film as a FM electrode instead of LSMO is expected to change TAMR behaviors clearly. This is because recent study reported that the magnetization easy axis of Co is changed from in-plane direction to out-of-plane direction because of charge transfer at the interface between C_{60} and Co thin film.[103]

6.3.3 Study on the correlation between Hanle effects and spinterface

To observe Hanle effect in nonlocal spin valve, which is a change of nonlocal MR based on a spin precession by perpendicular magnetic field, is important to study spin transport. However, some groups have described reasons for suppression of Hanle effect in organic spin valves (e.g. low mobility of OMs,[88] large TMR/TAMR effect[69] and fast spin transport in OMs[78]). In my study, I also could not observe Hanle effect for α-I_3 single crystal in chapter 4 probably because of long spin lifetime or fast spin transport in α-I_3.

I would like to suggest Hanle effect may be also suppressed by the appearance of perpendicular magnetization at the interface between FM and OMs. To observe clear Hanle effect, it is necessary to apply perpendicular magnetic field against electron spins injected from FM. However, if there is out-of-plane easy axis of magnetization, as like Co/C_{60} interface,[103] it is difficult to apply perpendicular magnetic field against electron spin direction. This is because interface magnetization points easily along magnetic field. Consequently, electron spins injected from the FM interface are also parallel to magnetic field, and the spin precession does not occur.

The TAMR measurements in chapter 5 and the previous study[113] indicated that one can get information about magnetization direction at the interface from TAMR behaviors. To elucidate the direction of electron spins injected from the interface will

promote the understanding of spin transport in OMs (e.g. the origin of suppression of Hanle effect).

Reference

[1] S. Bandyopadhyay and M. Cahay, *INTRODUCTION TO Spintronics*, CRC Press (2008).

[2] J. M. Kikkawa and D. D. Awschalom, *Nature*, **397**, 139 (1999).

[3] R. Fiederling, M. Keim, G. Reuscher, W. Ossau, G. Schmidt, A. Waag and L. W. Molenkamp, *Nature*, **402**, 787 (1999).

[4] K. Uchida, S. Takahashi, K. Harii, J. Ieda, W. Koshibae, K. Ando, S. Maekawa and E. Saitoh Nature, **455**, 778 (2008).

[5] K. Uchida, H. Adachi, T. Ota, H. Nakayama, S. Maekawa, and E. Saitoh, *Appl. Phys. Lett.* **97**, 172505 (2010).

[6] E. Saitoh, M. Ueda, and H. Miyajima G. Tatara, *Appl. Phys. Lett*, **88,** 182509 (2006)**.**

[7] K. Ando, S. Takahashi, J. Ieda, Y. Kajiwara, H. Nakayama, T. Yoshino, K. Harii, Y. Fujikawa, M. Matsuo, S. Maekawa and E. Saitoh, *J. Appl. Phys*. **109**, 103913 (2011).

[8] M. N. Baibich, J. M. Broto, A. Fert, F. Nguyen Van Dau and F. Petroff, *Phys. Rev. Lett.* **61**, 2472 (1988).

[9] G. Binasch, P. Grünberg, F. Saurenbach and W. Zinn, *Phys. Rev. B* **39**, 4828 (1989).

[10] W. Thomson, *Proc. Royal. Soc. London* **8**, 546 (1856).

[11] S. Miwa, S. Ishibashi, H. Tomita, T. Nozaki, E. Tamura, K. Ando, N. Mizuochi, T. Saruya, H. Kubota, K. Yakushiji, T. Taniguchi, H. Imamura, A. Fukushima, S. Yuasa and Y. Suzuki, *Nature Mater.* **13**, 50 (2014).

[12] S. Datta and B. Das, *Appl. Phys. Lett.* **56**, 665 (1990).

[13] D. Sun, E. Ehrenfreund and Z. V. Vardeny, *Chem. Commun*, **50**, 1781 (2014).

[14] N. F. Mott, *Proc. R. Soc. London, Ser. A,* **156**, 699 (1936).

[15] G. Schmidt, *J. Phys. D: Appl. Phys*. **38**, R107 (2005).

[16] T. Wakamura, N. Hasegawa, K. Ohnishi, Y. Niimi and Y. Otani, *Phys. Rev, Lett.* **112**, 036602 (2014).

[17] K. Taguchi, T. Yokoyama and Y. Tanaka, *Phys. Rev. B* **89**, 085407 (2014).

[18] M, Shiraishi, *Jpn. J. Appl. Phys.* **51**, 08KA01 (2012).

[19] T. Matsuno, S. Sugahara, and M. Tanaka, *Jpn. J. Appl. Phys.* **43**, 6032 (2004).

[20] W. J. M. Naber, S. Faez and W. G. van der Wiel, *J. Phys. D: Appl. Phys*. **40**, R205

(2007).

[21] V. Dediu, M. Murgia, F. C. Matacotta, C. Talian and S. Barbanera, *Solid State Commun.* **122**, 181 (2002).

[22] Z. H. Xiong, D. Wu, Z. V. Vardeny and J. Shi, *Nature* **427,** 821 (2004).

[23] K. Tsukagoshi, B. W. Alphenaar and H. Ago, *Nature* **401**, 572 (1999).

[24] A. H. Davisa and K. Bussmann, *J. Appl. Phys.* **93**, 7358 (2003).

[25] G. Salis, S. F. Alvarado, M. Tschudy, T. Brunschwiler, and R. Allenspach, *Phys. Rev. B* **70**, 085203 (2004).

[26] T. D. Nguyen, E. Ehrenfreund and Z. V. Vardeny, *Science* **337**, 204 (2012).

[27] B. Ding, Q. Song and K. Alameh, *Appl. Phys. Lett.* **104**, 203302 (2014).

[28] J.-W. Yoo, C.-Y. Chen, H.W. Jang, C.W. Bark, V. N. Prigodin, C. B. Eom and A. J. Epstein, *Nature Mater.* **9**, 638 (2010).

[29] B. Li, C.-Y. Kao, J.-W. Yoo, V. N. Prigodin and A. J. Epstein, *Adv. Mater.* **23**, 3382 (2011).

[30] M. Prezioso, A. Riminucci, I. Bergenti, P. Graziosi, D. Brunel and V. A. Dediu, *Adv. Mater.* **23**, 1371 (2011).

[31] M. Prezioso, A. Riminucci, P. Graziosi, I. Bergenti, R. Rakshit, R. Cecchini, A. Vianelli, F. Borgatti, N. Haag, M. Willis, A. J. Drew, W. P. Gillin and V. A. Dediu, *Adv. Mater.* **25**, 534 (2013).

[32] J. H. Park, E. Vescovo, H. J. Kim, C. Kwon, R. Ramesh and T. Venkatesan, *Phys. Rev. Lett*. **81**, 1953 (1988).

[33] C. Barraud, P. Seneor, R. Mattana, S. Fusil, K. Bouzehouane, C. Deranlot, P. Graziosi, L. Hueso, I. Bergenti, V. Dediu, F. Petroff and A. Fert, *Nat. Phys.* **6**, 615 (2010).

[34] R. Lin, F. Wang, M. Wohlgenannt, C. He, X. Zhai, and Y. Suzuki, *Synth. Met.* **161**, 553 (2011).

[35] T. L. A. Tran, T. Q. Le, J. G. M. Sanderink, W. G. van der Wiel and M. P. de Jong, *Adv. Funct. Mater*. **22**, 1180 (2012).

[36] E.P. Yelsukov, E.V. Voronina and V.A. Barinov, *J. Magn. Magn. Mater.* **115**, 271 (1992).

[37] C. M. Schneider, P. Bressler, P. Schuster, J. Kirschner, J. J. de Miguel and R. Miranda, *Phys. Rev. Lett.* **64**, 1059 (1990).

[38] A. J. Drew, J. Hoppler, L. Schulz, F. L. Pratt, P. Desai, P. Shakya, T. Kreouzis, W. P.

Gillin, A. Suter, N. A. Morley, V. K. Malik, A. Dubroka, K.W. Kim, H. Bouyanfif, F. Bourqui, C. Bernhard, R. Scheuermann, G. J. Nieuwenhuys, T. Prokscha and E. Morenzoni, *Nature Mater.* **8**, 109 (2009).

[39] B. B. Chen, Y. Zhou, S. Wang, Y. J. Shi, H. F. Ding and D. Wu, *Appl. Phys. Lett.* **103**, 072402 (2013).

[40] C. B.-Bin, J. S.-Wei, D. H.-Feng, J. Z.-Sheng and W. Di, *Chin. Phys. B* **23**, 018104 (2014).

[41] S.W. Jiang, S. Liu, P. Wang, Z. Z. Luan, X. D. Tao, H. F. Ding and D. Wu, *Phys. Rev. Lett*. **115**, 086601 (2015).

[42] P. A. Bobbert, W. Wagemans, F.W. A. van Oost, B. Koopmans and M. Wohlgenannt, *Phys. Rev. Lett*. **102**, 156604 (2009).

[43] Z. G. Yu, *Phys. Rev. Lett*. **106**, 106602 (2011).

[44] Z. G. Yu, *Phys. Rev. B* **85**, 115201 (2012).

[45] T. D. Nguyen, G. Hukic-Markosian, F. Wang, L. Wojcik, X. Li, E. Ehrenfreund and Z. V. Vardeny, *Nature Mater.* **9**, 345 (2010).

[46] Tho D. Nguyen, T. P. Basel, Y.-J. Pu, X-G. Li, E. Ehrenfreund and Z. V. Vardeny, *Phys. Rev. B* **85**, 245437 (2012).

[47] S. Majumdara and H. S. Majumdarb, *Synth. Met.* **173**, 26 (2013).

[48] F. Li, T. Li, F. Chen and F. Zhang, *Sci. Rep.* **5**, 9355 (2015).

[49] S. W. Jiang, P. Wang, B. B. Chen, Y. Zhou, H. F. Ding and D. Wu, *Appl. Phys. Lett*. **107**, 042407 (2015).

[50] P. P. Ruden and D. L. Smith, J. Appl. Phys. **95**, 4898 (2004).

[51] S. MajumdarR. LaihoP. Laukkanen and I. J. VäyrynenHimadri S. Majumdar and R. Österbacka, *Appl. Phys. Lett*. **89**, 122114 (2006).

[52] X. Zhang, S. Mizukami, T. Kubota1, Q. Ma1, M. Oogane, H. Naganuma, Y. Ando and T Miyazaki, *Nature Commun.* **4**, 1392 (2013).

[53] Y. S. Dedkov, U. Rüdiger and G. Güntherodt, *Phys. Rev. B* **65**, 064417 (2002).

[54] H. Xiang, F. Shi, M. S. Rzchowski, P. M. Voyles and Y. Austin Chang, *Appl. Phys. Lett.* **97**, 092508 (2010).

[55] Y. Kawasugi, T. Ujino, H. Tada, *Org. Electro.* **14**, 3186 (2013).

[56] M. Jourdan, J. Minár, J. Braun, A. Kronenberg, S. Chadov, B. Balke, A. Gloskovskii, M. Kolbe, H. J. Elmers, G. Schönhense, H. Ebert, C. Felser, M. Kläui, *Nature Commun.*

5, 3974. (2014).

[57] P. J. Brown, K. U. Neumann, P .J. Webster and K. R. A. Ziebeck, *J. Phys.: Condens. Matter* **12**, 1827 (2000).

[58] T. S. Santos, J. S. Lee, P. Migdal, I. C. Lekshmi, B. Satpati and J. S. Moodera, *Phys. Rev. Lett.* **98**, 016601 (2007).

[59] J. H. Shim, K.V. Raman, Y. J. Park, T. S. Santos, G. X. Miao, B. Satpati, and J. S. Moodera, *Phys. Rev. Lett.* **100**, 226603 (2008).

[60] H. Vinzelberg, J. Schumann, D. Elefant, R. B. Gangineni, J. Thomas and B. Büchner, *J. Appl. Phys*. **103**, 093720 (2008).

[61] V. Dediu, L. E. Hueso, I. Bergenti, A. Riminucci, F. Borgatti, P. Graziosi, C. Newby, F. Casoli, M. P. De Jong, C. Taliani, and Y. Zhan, *Phys. Rev. B* **78**, 115203 (2008).

[62] S. Majumdar, H. S. Majumdar, R. Laiho and R. Österbacka, *New J. Phys.* **11**, 01302 (2009).

[63] D. Sun, L. Yin, C. Sun, H. Guo, Z. Gai, X.-G. Zhang, T. Z. Ward, Z. Cheng and J. Shen, *Phys. Rev. Lett.* **104**, 236602 (2010).

[64] P. M. Tedrow and R. Meservey, *Phys. Rev. B* **7**, 318 (1973).

[65] S. Sanvito, *Nature Phys*. **6**, 562 (2010).

[66] W. Xu, G. J. SzulczewskiP. LeClair, I. Navarrete, R. SchadG. Miao, H. Guo, and A. Gupta, *Appl. Phys. Lett.* **90**, 072506 (2007).

[67] J. S. Jiang, J. E. Pearson, and S. D. Bader, *Phys. Rev. B* **77**, 035303 (2008).

[68] M. Grünewald, M. Wahler, F. Schumann, M. Michelfeit, C. Gould, R. Schmidt, F. Würthner, G. Schmidt and L. W. Molenkamp, *Phys. Rev. B* **84**, 125208 (2011).

[69] M. Grünewald, R. Göckeritz, N. Homonnay, F. Würthner, L. W. Molenkamp and G. Schmidt, *Phys. Rev. B* **88**, 085319 (2013).

[70] K. V. Raman, A. M. Kamerbeek, A. Mukherjee, N. Atodiresei, T. K. Sen, P. Lazić, V. Caciuc, R. Michel, D. Stalke, S. K. Mandal, S. Blügel, M. Münzenberg and J. S. Moodera, *Nature* **493**, 509 (2013).

[71] K. Ando, S. Watanabe, S. Mooser, E. Saitoh and H. Sirringhaus, *Nature Mater*. **12**, 622 (2013).

[72] S. Watanabe, K. Ando, K. Kang, S. Mooser, Y. Vaynzof, H. Kurebayashi, E. Saitoh and H. Sirringhaus, *Nature Phys*. **10**, 308 (2014).

[73] J.-W. Yoo, H.W. Jang, V.N. Prigodin, C. Kao, C.B. Eom, A.J. Epstein, *Synth. Met*.

160, 216 (2010).

[74] R. Lin, F. Wang, J. Rybicki, and M. Wohlgenannt, *Phys. Rev. B*, **81**, 195214 (2010).

[75] J. J. H. M. Schoonus, P. G. E. Lumens, W. Wagemans, J. T. Kohlhepp, P. A. Bobbert, H. J. M. Swagten and B. Koopmans, *Phys. Rev. Lett.*, **103**, 146601 (2009).

[76] J. Rybicki, R. Lin, F. Wang, M. Wohlgenannt, C. He, T. Sanders and Y. Suzuki, *Phys. Rev. Lett.*, **109**, 076603 (2012).

[77] M. Cinchetti, K. Heimer, J.-P. Wüstenberg, O. Andreyev, M. Bauer, S. Lach, C. Ziegler, Y. Gao and M. Aeschlimann, *Nature Mater.* **8**, 115 (2009).

[78] Z. G. Yu, *Phys. Rev. Lett.*, **111**, 016601 (2013).

[79] Z. G. Yu, *Nature Commun.* **5**, 4842 (2014).

[80] D. Sun, K. J. van Schooten, M. Kavand, H. Malissa, C. Zhang, M. Groesbeck, C. Boehme and Z. V. Vardeny, *Nature Mater.* **15**, 863 (2016).

[81] B. B. Chen, S. Wang, S. W. Jiang, Z. G. Yu, X. G. Wan, H. F. Ding and D. Wu, *New J. Phys*. **17**, 013004 (2015).

[82] T. D. Nguyen, F. Wang, X.-G. Li, E. Ehrenfreund and Z. V. Vardeny, *Phys. Rev. B* **87**, 075205 (2013).

[83] P. K. Muduli, Gyanendra Singh, R. Sharma, and R. C. Budhani *J. Appl. Phys.* **105**, 113910 (2009).

[84] T. D. Nguyen, B. R. Gautam, E. Ehrenfreund and Z.V. Vardeny, *Phys. Rev. Lett.*, **105**, 166804 (2010).

[85] Z. G. Yu, *Nanoelectron. Spintron.* **1** 1 (2015).

[86] M. Johnson and R. H. Silsbee, *Phys. Rev. B* **37**, 5312 (1988).

[87] F. J. Jedema, H. B. Heersche, A. T. Filip, J. J. A. Baselmans and B. J. van Wees, *Nature* **416**, 713 (2002).

[88] A. Riminucci, M. Prezioso, C. Pernechele, P. Graziosi, I. Bergenti, R. Cecchini, M. Calbucci, M. Solzi, and V. A. Dediu, *Appl. Phys. Lett*. **102**, 092407 (2013).

[89] F. J. Jedema, A. T. Filip and B. J. van Wees, *Nature* **410**, 345 (2001).

[90] J. Devkota, R. Geng, R. C. Subedi and T. D. Nguyen, *Adv. Funct. Mater.* **26**, 3881 (2016).

[91] H. Idzuchi, Y. Fukuma and Y. Otani, *Physica E* **68,** 239 (2015).

[92] T. Sasaki, T. Oikawa, T. Suzuki, M. Shiraishi, Y. Suzuki and K. Tagami, *Appl. Phys. Express* **2**, 053003 (2009).

[93] H.-J. Jang and I. Appelbaum, *Phys. Rev. Lett.* **103**, 117202 (2009).

[94] M. Kameno, Y. Ando, T. Shinjo, H. Koike, T. Sasaki, T. Oikawa, T. Suzuki and M. Shiraishi, *Appl. Phys. Lett*. **104**, 092409 (2014).

[95] N. Tombros, C. Józsa, M. Popinciuc, H. T. Jonkman and B. J. van Wees, *Nature* **448,** 571 (2007).

[96] T. Maassen, F. K. Dejene, M. H. D. Guimarães, C. Józsa, and B. J. van Wees, *Phys. Rev. B* **83,** 115410 (2011).

[97] T. Maassen, J. J. van den Berg, N. IJbema, F. Fromm, T. Seyller, R. Yakimova and B. J. van Wees, *Nano Lett.* **12,** 1498 (2012).

[98] P. J. Zomer, M. H. D. Guimarães, N. Tombros and B. J. van Wees, *Phys. Rev. B* **86,** 161416(R) (2012).

[99] Y. Kawasugi, M. Ara, H. Ushirokita, T. Kamiya and H. Tada, *Org. Electron.* **14**, 1869 (2013).

[100] T. V. A. G. de Oliveira, M. Gobbi, J. M. Porro, L. E. Hueso and A. M. Bittner, *Nanotechnology* **24**, 475201 (2013).

[101] S. Zanettini, G. Chaumy, P. Chavez, N. Leclerc, C. Etrillard, B. Leconte, F. Chevrier, J.-F Dayen and B. Doudin, *J. Phys.: Condens. Matter* **27**, 462001 (2015).

[102] V. E. Campbell, M. Tonelli, I. Cimatti, J.-B. Moussy, L. Tortech, Y. J. Dappe, E. Rivière, R. Guillot, S. Delprat, R. Mattana, P. Seneor, P. Ohresser, F. Choueikani, E. Otero, F. Koprowiak, V. G. Chilkuri, N. Suaud, N. Guihéry, A. Galtayries, F. Miserque, M.-A. Arrio, P. Sainctavit and T. Mallah, Nature Commun. **7**, 13646 (2016).

[103] K. Bairagi, A. Bellec, V. Repain, C. Chacon, Y. Girard, Y. Garreau, J. Lagoute, S. Rousset, R. Breitwieser, Y. C. Hu, Y. C. Chao, W. W. Pai, D. Li, A. Smogunov and C. Barreteau, *Phys. Rev. Lett.* **114**, 247203 (2015).

[104] F. Al Ma'Mari, T. Moorsom, G. Teobaldi, W. Deacon, T. Prokscha, H. Luetkens, S. Lee, G. E. Sterbinsky, D. A. Arena, D. A. MacLaren, M. Flokstra, M. Ali, M. C. Wheeler, G. Burnell, B. J. Hickey and O. Cespedes, *Nature* **524**, 69 (2015).

[105] F. Djeghloul, M. Gruber, E. Urbain, D. Xenioti, L. Joly, S. Boukari, J. Arabski, H. Bulou, F. Scheurer, F. Bertran, P. Le Fèvre, A. T.-Ibrahimi, W. Wulfhekel, G. Garreau, S. H.-Garreau, P. Wetzel, M. Alouani, E. Beaurepaire, M. Bowen and W. Weber, *J. Phys. Chem. Lett.* **7**, 2310 (2016).

[106] F.J. Wang, Z.H. Xiong, D. Wu, J. Shi, Z.V. Vardeny, *Synth. Met*. **155**, 172 (2005).

[107] F. J. Wang, C. G. Yang, Z. V. Vardeny, and X. G. Li, *Phys. Rev. B* **75**, 245324 (2007).

[108] J. J. H. M. Schoonus, P. G. E. Lumens, W. Wagemans, J. T. Kohlhepp, P. A. Bobbert, H. J. M. Swagten, and B. Koopmans, *Phys. Rev. Lett.* **103**, 146601 (2009).

[109] X. Sun, A. B.-Pinto, R. Llopis, F. Casanova and L. E. Hueso, *Appl. Phys. Lett*. **105**, 083302 (2014).

[110] X. Zhang, Q. Ma, K. Suzuki, A. Sugihara, G. Qin, T. Miyazaki and S. Mizukami, *ACS Appl. Mater. Interfaces*, **7**, 4685 (2015).

[111] C. Barraud, K. Bouzehouane, C. Deranlot, D. J. Kim, R. Rakshit, S. Shi, J. Arabski, M. Bowen, E. Beaurepaire, S. Boukari, F. Petroff, P. Seneor and R. Mattana, *Dalton Trans.*, **45**, 16694 (2016).

[112] S. Takahashi and S. Maekawa, *Phys. Rev. B* **67**, 052409 (2003).

[113] C. Barraud, K. Bouzehouane, C. Deranlot, S. Fusil, H. Jabbar, J. Arabski, R. Rakshit, D. J. Kim, C. Kieber, S. Boukari, M. Bowen, E. Beaurepaire, P. Seneor, R. Mattana and F. Petroff, *Phys. Rev. Lett*. **114**, 206603 (2015).

[114] H. Idzuchi, Y. Fukuma and Y. Otani, *Sci. Rep,* **2,** 628 (2012).

[115] M. H. D. Guimarães, P. J. Zomer, J. Ingla-Aynés, J. C. Brant, N. Tombros, and B. J. van Wees, *Phys. Rev. Lett.* **113**, 086602 (2014).

[116] T. V. A. G. de Oliveira, M. Gobbi, J. M. Porro, L. E. Hueso and A. M. Bittner, *Nanotechnology* **24**, 475201 (2013).

[117] O. M. J. van't Erve, A. T. Hanbicki, M. Holub, C. H. Li, C. Awo-Affouda, P. E. Thompson and B. T. Jonker, *Appl. Phys. Lett.* **91**, 212109 (2007).

[118] A. J. Heeger, S. Kivelson, J. R. Schrieffer and W.-P. Su, *Rev. Mod. Phys.* **60**, 781 (1988).

[119] K. Bender, I. Hennig, D. Schweitzer, K. Dietz, H. Endres and H. J. Keller, *Mol. Cryst. Liq. Cryst.* **108**, 359 (1984).

[120] N. Tajima, S. Sugawara, M. Tamura, Y. Nishio and K. Kajita, *J. Phys. Soc. Jpn.* **75,** 051010 (2006).

[121] N. Tajima, S. Sugawara, M. Tamura, Y. Nishio and K. Kajita, *Europhys. Lett.* **80,** 47002 (2007).

[122] Y. Kawasugi, H. M. Yamamoto, M. Hosoda, N. Tajima, T. Fukunaga, K. Tsukagoshi, and R. Kato, *Appl. Phys. Lett*., **92**, 243508 (2008).

[123] N. Tajima, T. Yamauchi, T. Yamaguchi, M. Suda, Y. Kawasugi, H. M. Yamamoto, R. Kato, Y. Nishio and K. Kajita, *Phys. Rev. B* **88,** 075315 (2013).

[124] F. J. Jedema, M. S. Nijboer, A. T. Filip and B. J. van Wees, *Phys. Rev. B* **108**, 359, 085319 (2013).

[125] W. Han, R. K. Kawakami, M. Gmitra and J. Fabian, *Nature Nanotechnol*. **9**, 794 (2014).

[126] C. Józsa, T. Maassen, M. Popinciuc, P. J. Zomer, A. Veligura, H. T. Jonkman and B. J. van Wees, *Phys. Rev. B* **80,** 241403(R) (2009).

[127] T. Maassen, F. K. Dejene, M. H. D. Guimarães, C. Józsa, and B. J. van Wees, *Phys. Rev. B* **83,** 115410 (2011).

[128] H. Idzuchi, A. Fert, and Y. Otani, *Phys. Rev. B* **91**, 241407 (2015).

[129] D. Huertas-Hernando, F. Guinea and A. Brataas, *Phys. Rev. B* **74,** 155426 (2006).

[130] P. Zhang and M. W. Wu, *New J. Phys.* **14,** 033015 (2012).

[131] B. Dlubak, M.-B. Martin, C. Deranlot, B. Servet, S. Xavier, R. Mattana, M. Sprinkle, C. Berger, W. A. De Heer, F. Petroff, A. Anane, P. Seneor and A. Fert1 *Nature Physics* **8,** 557 (2012).

[132] V. Dediu, L. Hueso, I. Bergenti and C. Taliani, *Nature Mater.* **8**, 707 (2009).

[133] S. Lach, A. Altenhof, K. Tarafder, F. Schmitt, M. Ali, M. Vogel, J. Sauther, P. M. Oppeneer and C. Ziegler, *Adv. Funct. Mater.* **22**, 989 (2012).

[134] F. Djeghloul, F. Ibrahim, M. Cantoni, M. Bowen, L. Joly, S. Boukari, P. Ohresser, F. Bertran, P. L. Fèvre, P. Thakur, F. Scheurer, T. Miyamachi, R. Mattana, P. Seneor, A. Jaafar, C. Rinaldi, S. Javaid, J. Arabski, J. P. Kappler, W. Wulfhekel, N. B. Brookes, R. Bertacco, A. T. Ibrahimi, M. Alouani, E. Beaurepaire and W. Weber, *Sci. Rep*. **3**, 1272 (2013).

[135] O. B. Dor, S. Yochelis, S. P. Mathew, R. Naaman and Y. Paltiel, *Nat. Commun.* **4**, 2256 (2013).

[136] D. Sun, W. M. Fang, X. Xu, L. Jiang, H. Guo, Y. Wang, W. Yang, L. Yin, P. C. Snijders, T. Z. Ward, Z. Gai, X. G. Zhang, H. N. Lee and J. Shen, *Nat. Commun*. **5**, 4396 (2014).

[137] T. Moorsom, M. Wheeler, T. M. Khan, F. A. Ma'Mari, C. Kinane, S. Langridge, D. Ciudad, A. B. Pinto, L. Hueso, G. Teobaldi, V. K. Lazarov, D. Gilks, G. Burnell, B. J.

Hickey and O. Cespedes, *Phys. Rev. B* **90**, 125311 (2014).
[138] A. M. Abiague and J. Fabian, *Phys. Rev. B* **79,** 155303 (2009).
[139] C. Gould, C. Rüster, T. Jungwirth, E. Girgis, G. M. Schott, R. Giraud, K. Brunner, G. Schmidt and L. W. Molenkamp, *Phys. Rev. Lett.* **93**, 117203 (2004).
[140] C. Rüster, C. Gould, T. Jungwirth, J. Sinova, G. M. Schott, R. Giraud, K. Brunner, G. Schmidt and L. W. Molenkamp, *Phys. Rev. Lett.* **94**, 027203 (2005).
[141] L. Gao, X. Jiang, S. H. Yang, J. D. Burton, E. Y. Tsymbal and S. S. P. Parkin, *Phys. Rev. Lett.* **99,** 226602 (2007).
[142] S. Hatanaka, S. Miwa, K. Matsuda, K. Nawaoka, K. Tanaka, H. Morishita, M. Goto, N. Mizuochi, T. Shinjo and Y. Suzuki, *Appl. Phys. Lett.* **107**, 082407 (2015)
[143] K. Wang, J. G. M. Sanderink, T. Bolhuis, W. G. van der Wiel and M. P. de Jong, *Phys. Rev. B* **89**, 174419 (2014).
[144] M. Grünewald, N. Homonnay, J. Kleinlein and G. Schmidt, *Phys. Rev. B* **90**, 205208 (2014).
[145] J. D. Burton and E. Y. Tsymbal, *Phys. Rev. B* **93**, 024419 (2016).
[146] H. Boschker, M. Mathews, E. P. Houwman, H. Nishikawa, A. Vailionis, G. Koster, G. Rijnders and D. H. A. Blank, *Phys. Rev. B* **79**, 214425 (2009).
[147] H. Boschker, J. Kautz, E. P. Houwman, G. Koster, D. H. A. Blank and G. Rijnders, *J. Appl. Phys.* **108**, 103906 (2010).
[148] M. Huijben, L. W. Martin, Y.-H. Chu, M. B. Holcomb, P. Yu, G. Rijnders, D. H. A. Blank and R. Ramesh, *Phys. Rev. B* **78**, 094413 (2008).
[149] Y. Xu, M. Yamazaki and P. Villars, *Jpn. J. Appl. Phys.* **50**, 11RH02 (2011).
[150] M. Sayani, S. M. Himadri, L. Reino, and Ö. Ronald, New J. Phys. **11**, 013022 (2009)
[151] J. Moser, A. M. Abiague, D. Schuh, W. Wegscheider, J. Fabian and D. Weiss, *Phys. Rev. Lett*. **99**, 056601 (2007).

List of publications

Conference

● Takeshi Kamiya, Yoshitaka Kawasugi, Masato Ara and Hirokazu Tada. “Preparation of α-(BEDT-TTF)$_2$I$_3$ spin valve under pressure”, in JPS Spring Meeting, Japan (2012).

● Takeshi Kamiya, Yoshitaka Kawasugi, Masato Ara and Hirokazu Tada. “Non-local magnetoresistance in α-(BEDT-TTF)$_2$I$_3$ based spin valves”, in JPS Fall Meeting, Japan (2012)

● Takeshi Kamiya, Yoshitaka Kawasugi, Masato Ara and Hirokazu Tada. “Nonlocal spin valve measurement of organic conductors”, International Workshop of Computational Nano-Materials Design on Green Energy, Japan (2013).

● Takeshi Kamiya, Yoshitaka Kawasugi, Masato Ara and Hirokazu Tada. “Nonlocal magnetoresistance in α-(BEDT-TTF)$_2$I$_3$ based spin valves II -Study of AMR effects and spin injection-”, in JPS Spring Meeting, Japan (2013).

● Takeshi Kamiya, Yoshitaka Kawasugi, Masato Ara and Hirokazu Tada. “Evaluation of spin injection into organic conductor salts, α-(BEDT-TTF)$_2$I$_3$, by non-local spin valve measurements”, in JSAP Fall Meeting, Japan (2013).

● Takeshi Kamiya, Yoshitaka Kawasugi, Masato Ara and Hirokazu Tada. ”Nonlocal Magnetoresistance in Organic Spin Valves Based on an Organic Conductor α-(BEDT-TTF)$_2$I$_3$”, in Nano and Giga, USA (2014).

● Chihiro Miyahara, Takeshi Kamiya and Hirokazu Tada. “ Tunneling anisotropic magnetoresistance of $La_{0.67}Sr_{0.33}MnO_3$ and pentacene”, in JSAP Fall Meeting, Japan (2015).

● Takeshi Kamiya, Chihiro Miyahara and Hirokazu Tada. “Large tunneling anisotropic magnetoresistance at the interface of thin organic films and $La_{0.67}Sr_{0.33}MnO_3$ grown on $SrTiO_3$(110)”, in JSAP Fall Meeting, Japan (2016).

● Takeshi Kamiya, Chihiro Miyahara and Hirokazu Tada “Large anisotropic Magnetoresistance in Cu/pentacene/ $La_{0.67}Sr_{0.33}MnO_3$ stractures prepared on $SrTiO_3$(110)”, in ECMolS, Italy (2016).

Original paper

● Takeshi Kamiya, Chihiro Miyahara and Hirokazu Tada “Large Tunneling Anisotropic Magnetoresistance in $La_{0.7}Sr_{0.3}MnO_3$/Pentacene/Cu Structures Prepared on $SrTiO_3$ (110) Substrates”, *Appl. Phys. Lett*., **110**, 032401 (2017). DOI: 10.1063/1.4974079

● Takeshi Kamiya, Yoshitaka Kawasugi, Masato Ara and Hirokazu Tada “Nonlocal magnetoresistance measurements of organic zero-gap conductor α-$(BEDT\text{-}TTF)_2I_3$”, *Phys*. *Rev. B*, **95**, 085307 (2017). DOI: 10.1103/PhysRevB.95.085307

●Yoshitaka Kawasugi, Masato Ara, Hiroaki Ushirokita, Takeshi Kamiya and Hirokazu Tada “Preparation of lateral spin-valve structure using doped conducting polymer poly(3,4-ethylenedioxythiophene) poly(styrenesulfonate)”, *Org. Electron.* **14**, 1869 (2013). DOI: 10.1016/j.orgel.2013.04.026

Acknowledgements

This thesis would not have been possible without his/her guidance and help that I wish to thank here.

First, I would like to express my sincere gratitude to my supervisor, Professor Hirokazu Tada, for providing me this precious study opportunity as a Ph.D student in his laboratory. His kindly comments, considerable suggestions and invaluable guidance are indispensable to learn in my student life.

I am grateful to Prof, Hiroshi Yoshida and Prof. Yoshishige Suzuki for accepting to referee this work.

I would like to express my appreciation to Dr. Yoshitaka Kawasugi (RIKEN) for his earnest guidance and discussion that make my research of great achievement. I am grateful to Associate Prof. Yamada, Dr. Ohto for their profound comments and suggestions.

I would like to express my thanks to Dr. Ara and Mis. Miyahara for their valuable cooperation in my experiments.

I would like to express my appreciation to Dr. Dediu and his group members (ISMN, Italy) for their meaningful discussions. I am grateful to Dr. Tanaka (NICT Advanced ICT research Institute) and Dr. Onomitsu (NTT basic research laboratory) for accepting me as a trainee. I am also very grateful to Prof. Jitsukawa and his group member (Division of Chemical Engineering, Osaka university) for their kindly guidance.

I am very grateful to the Interactive Materials Science Cadet Program (Osaka university) for making my Ph.D. study possible by the financial support and kindly guidance.

I would like to express my thanks to Dr. Ushirokita and Dr. nobusue, for valuable suggestion and help. I am grateful to Ms. Kamei, Ms. Inaba and Ms. Fujita for helping research activities in laboratory. I am also grateful to my lab mates for their suggestion and help in my experiments.

Finally, I would like to extend my indebtedness to my family for their understanding, support, encouragement and sacrifice throughout my study.